NUCLEAR INTERACTIONS IN A HIGH ENERGY MULTIPLATE CLOUD CHAMBER

Thesis by

Robert Lee Luttermoser

In Partial Fulfillment of the Requirements

For the Degree of

Doctor of Philosophy

California Institute of Technology

Pasadena, California

1963

ABSTRACT

A large multiplate cloud chamber, 5 feet x 5 feet x 2 feet, was built for the purpose of investigating high energy nuclear interactions. The chamber contained eleven (11) steel plates of absorbing material, totaling two hundred fifty-four (254) grams/(centimeter)^2.

The cross-section for the transfer of small amounts of energy by incident primary particles of high energy was obtained by direct mensuration on the stereoscopic photographic negatives. The tracks of high energy cosmic ray particles were identified by observation of events in which at least 50 Bev was observed in a high energy nuclear interaction. These same tracks were searched for nuclear interactions of less than 10 Bev.

The analysis of six hundred thirty-six (636) cases yielded a mean free path in iron for the primary particles in producing the small interactions of $(4.37 \pm 1.46) \times 10^3$ grams/(centimeter)^2. The primary particle-nucleus cross-section was 21.1 ± 7.1 millibarns, which corresponded to a primary particle-nucleon cross-section of 0.38 ± 0.13 millibarns. These events were interpreted as resulting from peripheral collisions of the primary particles with the nucleons of the iron nuclei.

An independent part of the analysis was the effect of the geiger counter efficiency. Results indicated an absence of bias in high energy cross-section measurements which were based on the assumption that the selection of events for measuring the cross-section was independent of the counter efficiency. However, analysis also showed that the establishment of symmetric errors in such a cross-section is probably misleading.

ACKNOWLEDGEMENTS

This thesis was written under the direction and with the encouragement of Nobel Laureate Carl D. Anderson and Dr. Eugene W. Cowan. The author wishes to express his sincere appreciation to them for the many helpful suggestions he was afforded during his research endeavor. The project was conceived in the fertile minds of his advisers and successfully guided by them to operational maturity.

Construction of the cloud chamber was undertaken with the help of capable draftsmen and machinists in the California Institute shop facilities. Acknowledgement is given the contribution of the technicians and former graduate students of the Cosmic Ray Group, who built the original circuitry and cameras, which were modified for this project. Particularly worthy of mention are the efforts of Mr. Keith Matthews, Mr. Bruce Dean, and Mr. Michael Suman for help in the construction and assembly of the equipment and in its subsequent operation.

The financial support of the Office of Naval Research, which funded the project, made this research possible. Appreciation is expressed to that office for its continued support of Cosmic Ray research at the California Institute of Technology.

TABLE OF CONTENTS

TABLE OF CONTENTS (CONTINUED)

LIST OF FIGURES

I. INTRODUCTION

Operation of the 8000 gauss 48-inch magnet in conjunction with a series of cloud chambers at the California Institute of Technology during the middle 1950's yielded many K meson and hyperon events resulting from nuclear interactions in a "heavi-met" (commercially available compressed tungsten) target. The limit of momentum analysis with that device was about 2 Bev/c. Endeavors by Dr. George H. Trilling to insert multiplates in one of the cloud chambers of the 48-inch magnet in order to investigate high energy nuclear events in excess of 2 Bev were not completely successful.

Because of the vacuous status of knowledge of interactions in the multi-Bev energy region, Drs. Carl D. Anderson and Eugene W. Cowan conceived a large cosmic ray cloud chamber as being the most fruitful means of investigation within the current state-of-the-art. Cost considerations rendered magnetic field momentum measurements impractical. Thus only statistical measurements of momentum from scattering were possible by the imposition at spaced intervals of high density absorbing material. Other gross phenomenological data, without detailed analysis on individual tracks, were obtainable by utilizing the theory of photon-electron cascade development and by the study of meson cones resulting from nuclear interactions.

The chamber that came into being was orders of magnitude larger than the original Wilson[1] cloud chamber of 7.5 centimeters in diameter and 4-5 millimeters in height. The new cloud chamber developed at that time

became the world's largest. In it photon-electron cascades were analyzable to an upper limit of about 10^5 Bev, assuming initiation of the shower in the first plate and the maximum occurring between the tenth and eleventh plates. The major research with the chamber, however, was not photon-electron showers, the theory for which is moderately well understood, but rather nuclear interactions caused by the impingement of the nucleons on a target of iron; i.e., one of the multiplates in the cloud chamber, or, alternatively, a low atomic number target material placed above the chamber.

Assembly of the chamber took place during early 1957 and preliminary pressure tests were undertaken on March 14, 1957. The chamber was expanded the first time on March 15 of that year and subsequent expansion and pressure tests were continued through the fall. Installation of the electronics was made by the author in December 1957 using the control chassis designed by Dr. Eugene W. Cowan for the 48-inch magnet cloud chambers. During the spring of 1958 additional control circuitry was made by Dr. Cowan and the author.

On July 28, 1958, installation of the steel multiplates began. The first picture with the multiplates under geiger counter control was made August 20, 1958.

Actual operation of the chamber began August 30, 1958, and except for minor shutdowns for cleaning it was essentially in operation continuously until July 25, 1961. The author assumed responsibility for the operation from March 15, 1959, until July 13, 1960. During the three years

of operation the chamber was recorded as expanding 103, 524 times. Thus even taking into account the expansions that were not photographed, over 100, 000 pictures were taken. The thesis presented herewith is based on the data of those photographs.

II. EXPERIMENTAL APPARATUS

The experimental apparatus consisted of (A) the Cloud Chamber Assembly, (B) the Electronic Controls, (C) an Optical System, and (D) External and Internal Targets. The laboratory instrumentation is shown in figure 1, page 5.

A. CLOUD CHAMBER ASSEMBLY

The cloud chamber, as shown in figure 2, page 6, was constructed of brass bars, 1 in. x 4 in. in cross-sectional area so as to form a frame 5 ft x 5 ft x 2 ft, with the 5-ft x 5-ft area in the vertical plane. This area was covered by a 1-1/4-in. tempered glass window through which observations of the events internal to the chamber were made. The 2-ft x 5-ft vertical sides also contained glass windows, four (4) in all, through which illumination of the chamber was obtained. The back vertical 5-ft x 5-ft area was a honeycomb aluminum piston which was originally black anodized. Later for improved optical contrast, a velvet-covered holey plate was placed in front of the piston. A 5-ft square neoprene rubber gasket between the piston and chamber exterior permitted movement of the piston through a total distance of 2 in. Such motion was effected by means of a compressing chamber to the rear of the piston. The compressing chamber was a 5-ft x 5-ft hollowed aluminum casting and contained compressed air thus keeping the cloud chamber in a normally compressed condition at an operating pressure between 16.5 and 19.0 centimeters of mercury. The neoprene rubber gasket acted as a seal between the cloud chamber and the

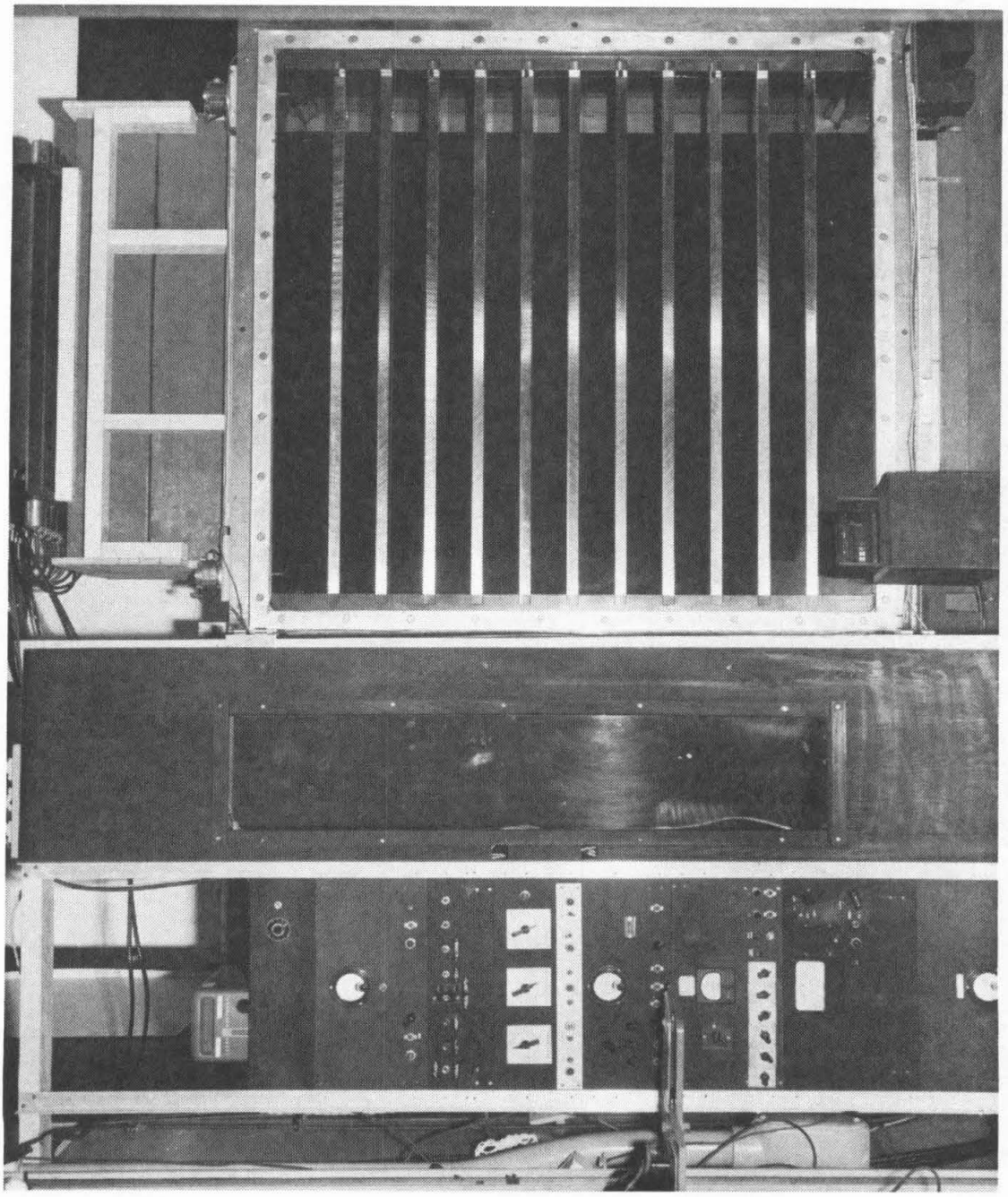

Figure 1. Laboratory Instrumentation

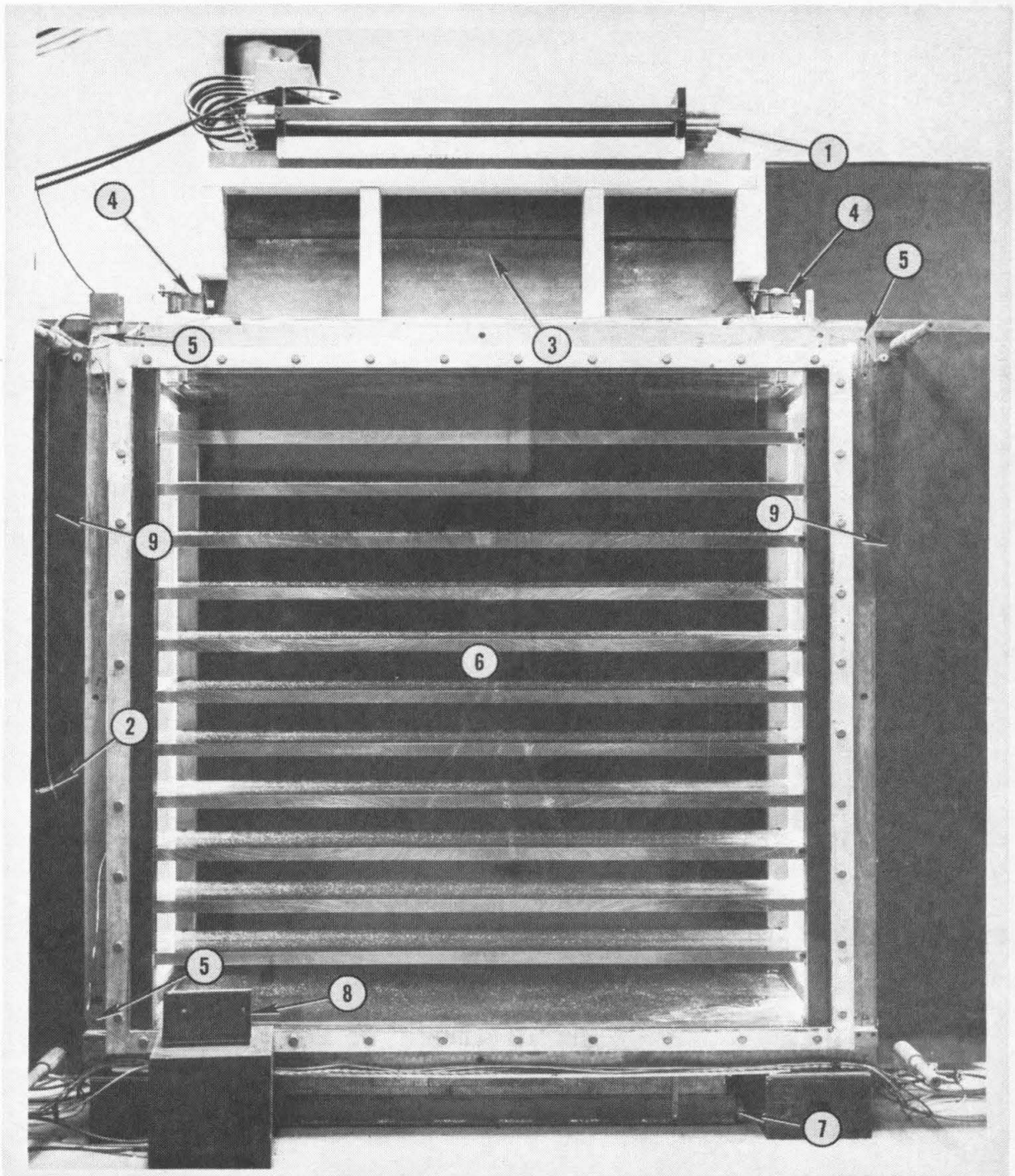

1 Geiger Tubes
2 Gas Input
3 Carbon Target
4 Fan Motors
5 Thermocouples
6 Cloud Chamber Containing 11 Steel Plates
7 Shielded Geiger Tubes
8 Data Box
9 Light Housing

Figure 2. Cloud Chamber

compressing chamber.

Control of the chamber was effected by an expansion mechanism on the rear of the compressing chamber. This device was the ingenious invention of Dr. Eugene W. Cowan. It consisted of a machined aluminum disk 16 in. in diameter with alternate radial segments ported together. One-half of these segments were ported directly to the compressing chamber by means of cuts through the disk, the other half of these segments consisted of chambers of shallow volume in the aluminum disk and were ported to a vacuum line. An annular rubber disk gasket covered all ports. In operation the vacuum ports pulled the rubber against the aluminum disk. Then compressed air was permitted to enter the compressing chamber through a valve mechanism. The rubber gasket was held in place, therefore, through but a delicate balance of vacuum and pressure on alternate segments, resulting in a rippled look circumferentially on the annular gasket. With compressed air in the compressing chamber, the piston was held forward. On appropriate electrical impulse a solenoid valve was released porting the vacuumed segments on the disk to the atmosphere, thus destroying the pressure balance on the gasket. Pressure internal to the cloud chamber then forced exhaustion of the compressing chamber. The rubber gasket which was held in place on its inner radius only was caused to rupture on its outer radius allowing the compressed air in the compressing chamber to escape to the atmosphere. The entire expansion took place in about 30 milliseconds, yielding the necessary adiabatic condition for the operation of the cloud chamber.

Restoration of the gasket to a sealed position against the aluminum disk was accomplished by two (2) alternate means. At first the compressed air was temporarily turned off and a second rapid action vacuum system was applied, this time to those ports which formerly were under pressure due to the compressed air. Thus both systems of ports temporarily were under vacuum and the rubber gasket was sealed to the aluminum disk. The second vacuum system was then turned off and air pressure restored to those ports putting the compressing chamber under pressure in excess of that of the cloud chamber and causing the piston to move forward.

This system was later abandoned in favor of a second means, a mechanical reset. Radially spaced steel springs forced the rubber gasket against the aluminum disk after an expansion had been completed. The springs were not of sufficient stiffness to prevent exhaustion of the compressing chamber under the pressure differential forcing its exhaustion.

The amount of forward motion of the piston in compression of the cloud chamber was limited and controlled by four (4) mechanisms, one (1) at each corner of the piston. The four controls were interconnected by a chain such that their drive screws all moved simultaneously by the same amount during adjustment. The driving screws had thirty-two (32) threads per inch and a total range of 2 in. They were used to adjust the expansion ratio of the chamber. By moving the chain, the screw position and thus a retaining stop attached to the screw was adjusted so as to limit the forward travel of the piston. When the piston reached its forward position in any particular corner, compressed air to the compressing chamber supplied

through a valve mechanism at that corner was shut off. Valves at all four corners had to be shut off in order to turn off the compressed air system to the compressing chamber. This procedure guaranteed that the piston was driven forward without cocking. A small leak was maintained in the compressing chamber as a further guarantee of the actuation of this safety mechanism.

Since the entire range of the screw was 2 in. compared to the cloud chamber depth of 2 ft an expansion ratio of 1.083 was possible when the cloud chamber contained only gas and vapor. This ratio was increased by virtue of some of the volume being occupied by the multiplates.

The chamber contained argon as the inert gas. An ethyl alcohol water mixture in a 3:1 ratio was used as the vapor. Approximately 235 cubic centimeters of liquid were required for saturation.

Early in the chamber operation endeavors were made to circulate the alcohol in the chamber by means of a pump. Liquid was squirted on the piston at two points through oscillating nozzles. Thus the alcohol wetted the piston completely enhancing the photographic background. It was felt that this system might prove satisfactory since the alcohol was sprayed at the top of the piston, minimizing the vapor density gradient from top to bottom of the chamber. Excessive condensation on the front glass, as shown in figure 7c, page 22, caused the circulating method to be abandoned, in spite of the attempts to cool the piston in an effort to prevent such condensation on the front glass.

Fan motors were installed in the upper portion of the chamber when

the circulation system was abandoned. Only the conventional small puddle of alcohol was maintained on the chamber floor. The fans were pulsed after each expansion for a period of 25 seconds to gain an equilibrium in the vapor saturation throughout the chamber. The former condensation problem was circumvented since the alcohol in excess of that necessary for chamber saturation was eliminated.

Thermal problems were not completely absent, however. A temperature control unit was built which was activated by a mercury thermal switch on the chamber. This switch could turn on an air conditioning unit or several commercial heaters placed in the room.

No endeavor was made to thermally drive any portion of the chamber. Instead it was permitted to seek its own equilibrium condition within the room. To further stabilize the room temperature an overriding thermostatic control was made by high-low thermostats placed outside the building to compensate for extremes in diurnal variation. Additionally during the summer months of operation a second air-conditioning unit was run continually in the room. The temperature at which the thermoswitch mounted on the chamber was actuated likewise was adjusted during the summer months.

To monitor thermal gradients in the chamber, thermocouples fed their output through a sampling switch to a galvanometer. Thus the temperature differences from front to rear, top to bottom, or left to right could be read each time the chamber was expanded for visual inspection.

B. ELECTRONIC CONTROLS

The electronic control system was housed primarily in a series of chassis in a vertical control panel shown in figure 3, page 12. The Thermocouple Monitor and Galvanometer were mounted at the top of the panel. Mounted below in order were the Sweep Field Chassis, the Auxiliary Control Chassis, the Main Control Chassis, the Geiger Coincidence Circuit, the Geiger Power Supply, the High Voltage Power Supply, and the main Power Supply.

The main power supply at the bottom of the rack supplied 300 volts regulated dc to the various chassis as shown in the block diagram, figure 4, page 13. It is to be noted that the power to actuate the thermal control system mentioned above was obtained directly from the 110- and 220-volt a-c mains.

The second chassis from the bottom was also an independent power supply, high voltage used in flashing the lights to take the pictures. The supply was used to charge a bank of forty 100-microfarad condensers which were maintained at a potential of 2000 volts dc.

The second chassis from the top of the control panel was an independent 600-volt power supply used as a sweep field during the developmental stages of the project before the multiplates were installed. Later by connecting alternate multiplates to ground it was possible to reduce the sweep field voltage to 225 volts applied to the opposite alternate set of plates. This latter voltage was supplied through the main control chassis.

The third chassis from the bottom was also an independent power

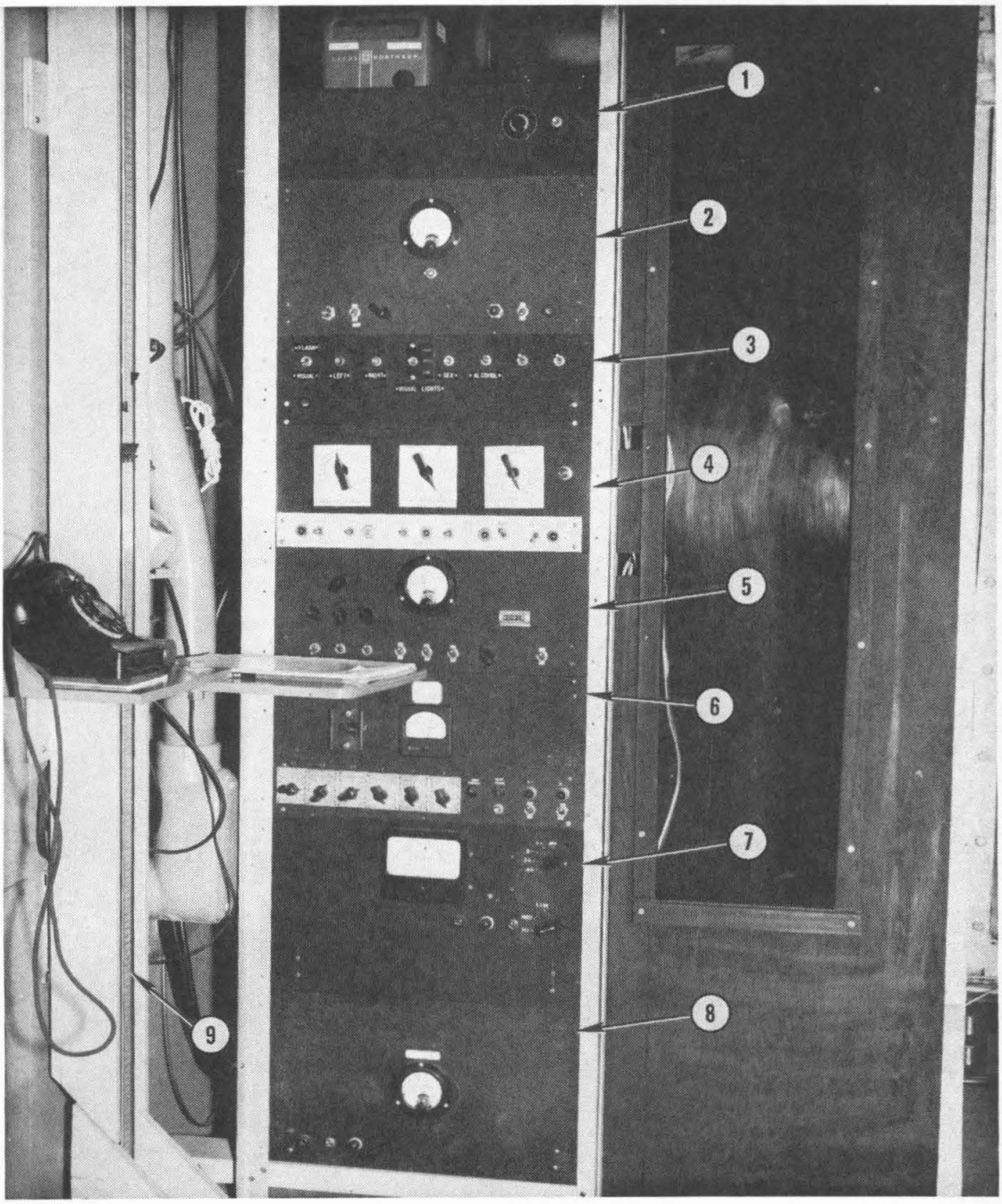

1 Thermocouple Monitor
2 Sweep Field Chassis
3 Auxiliary Control Chassis
4 Main Control Chassis
5 Geiger Coincidence Circuit
6 Geiger Power Supply
7 High Voltage Power Supply
8 Power Supply
9 Manometer

Figure 3. Electronic Control Panel

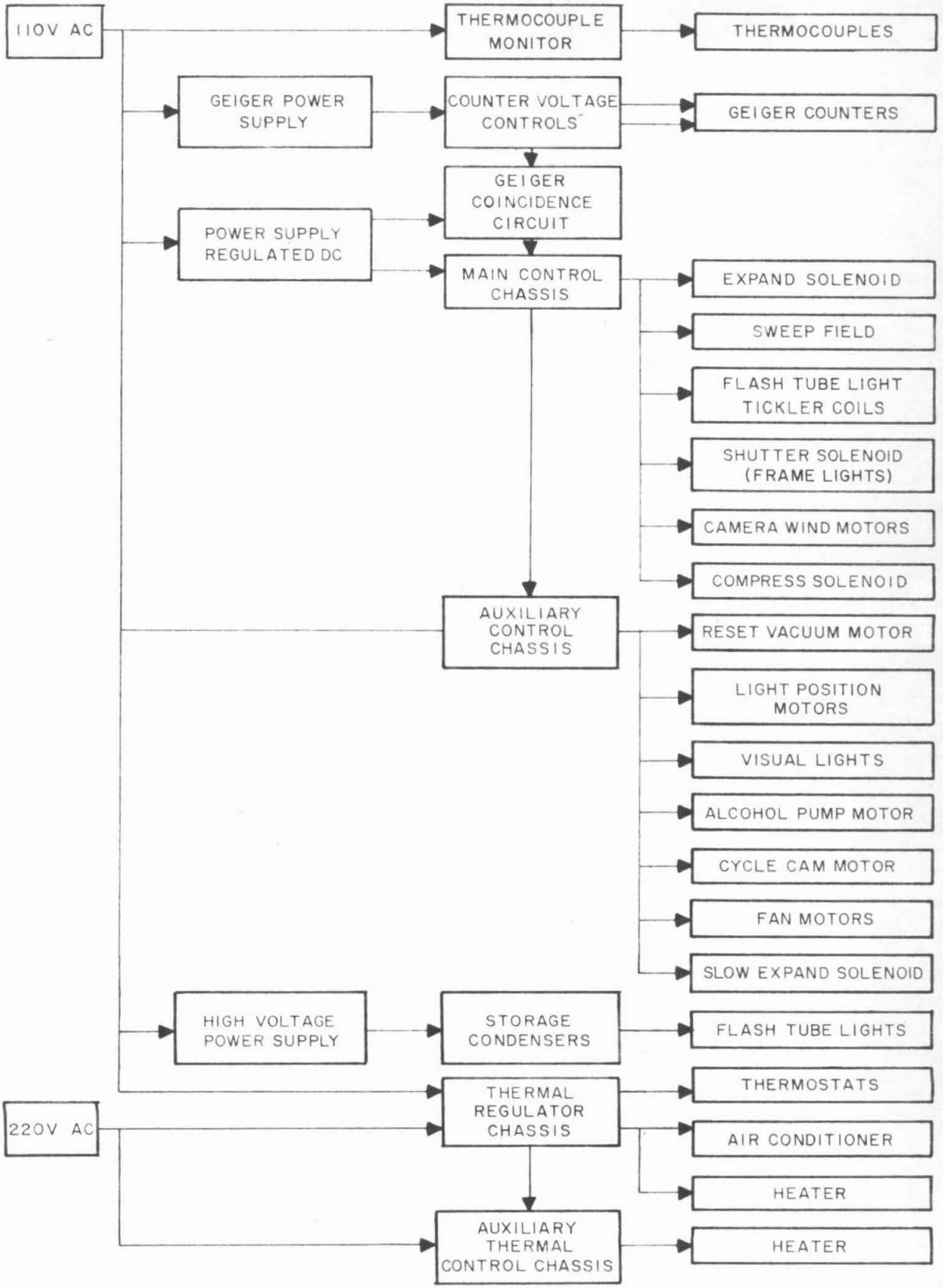

Figure 4. Block Diagram of Chamber Electronics

supply for the geiger counters. It was a 1300-volt regulated d-c supply and kept the three (3) banks of eight (8) geiger counters each at a high potential. Adjustment of individual geiger counter voltages was made by separate rheostats for each geiger counter. One (1) bank of geigers was placed directly above the chamber and two (2) directly below. Triggering of the cloud chamber was caused by a coincidence arrangement between the banks of geiger counters after the method originally introduced by Blackett and Occhialini[2]. After the installation of the carbon target on top of the chamber the geiger counters were placed above the carbon. Still later the upper tray was removed entirely so as to eliminate the bias against neutral primary events. At the same time lead, in addition to that already between the counters in the lower trays to prevent knock-on electron triggering, was supplemented by a lead brick stack behind the chamber. Some lead was also put in front of the chamber, but the stack of necessity was low in order to prevent visual obscuration from the vantage point of the camera. The purpose, of course, for the additional lead was to somewhat collimate to the vertical the angle of acceptance for triggering.

The geiger counters used were Radiation Counter Laboratory supplied cosmic ray counters, 2 in. in diameter and 42 in. long. Pulses from the counters actuated a 3-channel coincidence circuit which was the fifth (5th) chassis from the top of the rack. It was provided with adjustable bias which guaranteed that a given number of counters in a given bank had to be fired before actuation of a pulse to be used in coincidence with other

channels. A triggering investigation was undertaken, the results of which may be found in Appendix A.

The control system for the operation of the entire apparatus was maintained by means of the third and fourth chassis in the rack of electronics. The fourth chassis was modified from that used in a previous experiment. The fifth chassis was built for auxiliary control in this experiment. The pulse sequence generated by the two (2) control chassis is shown in figure 5, page 16.

When the geiger coincidence sequence was fulfilled a pulse was sent to the expand solenoid porting the vacuum segments on the expansion mechanism to the atmosphere as previously explained. Simultaneously the sweep field was turned off. After a delay of 150 milliseconds, which allowed sufficient time for droplet growth in the cloud chamber, the flash tube lights were pulsed. The shutter solenoid which controlled the data box frame lights was turned on for a period of 20 seconds. The alcohol pump motor used in the early stages of the project, as described above, was also on during this period.

When the pulse to the shutter solenoid ceased, a camera wind pulse was initiated, and maintained by a mechanical camera control on each camera separately for the time necessary to wind one (1) frame of film on the take-up spool. The same pulse also actuated the second vacuum system mentioned above by turning on the reset vacuum motor, thus exhausting the compressing chamber. The cycle cam motor was also initiated by this pulse, and was maintained on for three (3) minutes due to its own

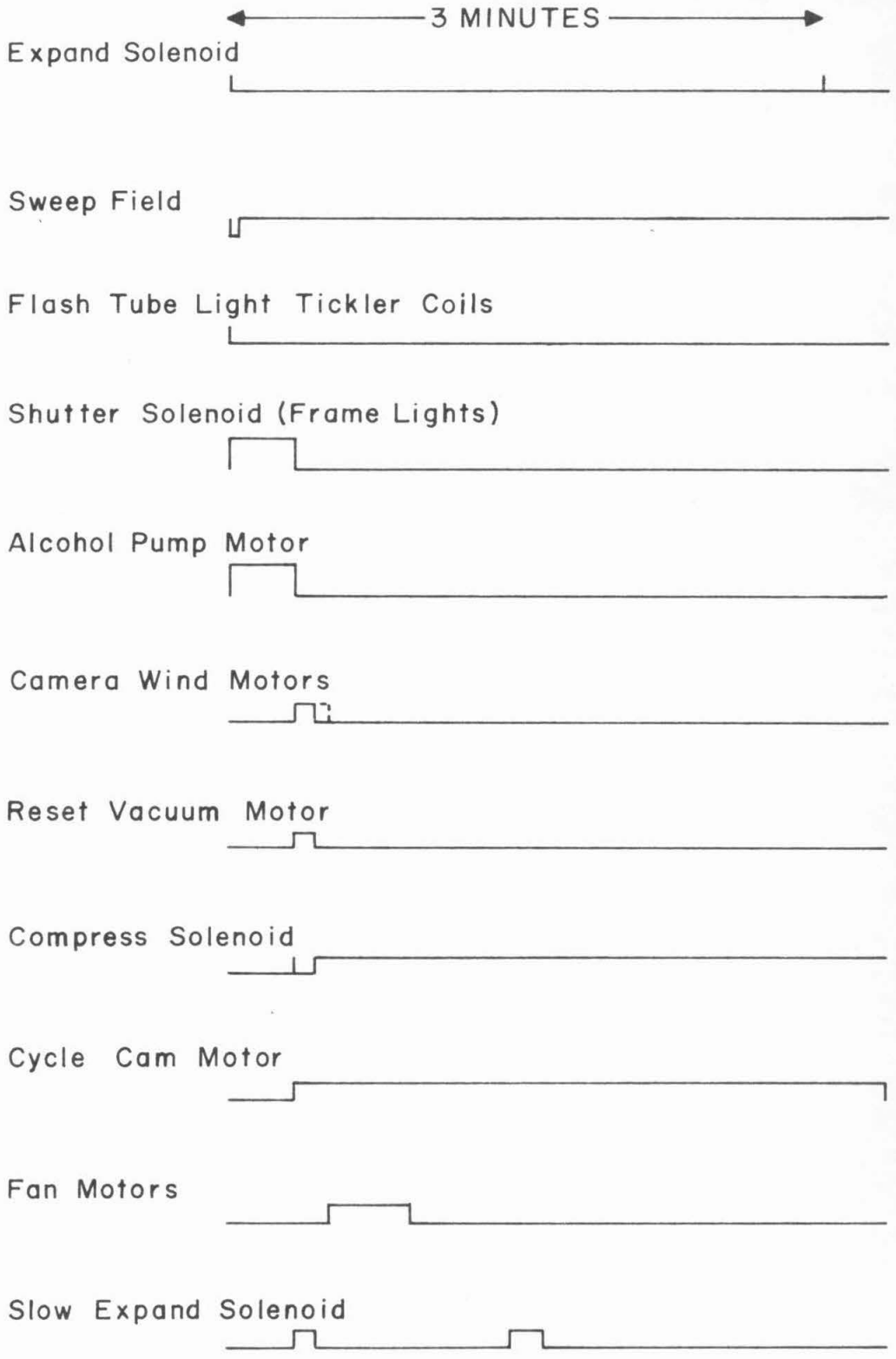

Figure 5. Pulse Sequence

internal microswitch system.

The cycle cam motor controlled the fan motor which agitated the gas in the chamber and the slow expand solenoid by means of supplemental cams controlling microswitches. As pointed out above the fan motors were pulsed after each expansion for approximately 25 seconds during the compression cycle. The compression actually was initiated at the close of the reset vacuum motor pulse even after the vacuum motor was abandoned as a reset means.

The slow expand solenoid likewise proved to be only a precautionary measure. It was not necessary to use it during the chamber operation. The 3-minute wait period, or hold time, proved sufficient for the chamber to come to equilibrium.

Additional circuitry not contained in the rack was a power supply and hodoscope originally designed for use in conjunction with geiger counters mounted on the ceiling of the room, for the purpose of investigating the radial extent of showers. This equipment illuminated a neon bulb, one for each counter, each time that counter was fired. If at the same time the chamber was fired the lights were held on, thus affording a photographic record of the circumstance at the time of firing. In the later operation of the experiment, the hodoscope was connected to the geiger counters below the chamber, rather than to the geiger counters attached to the ceiling. The purpose of this arrangement was to investigate possible triggering bias as a function of the point of initiation of nuclear showers in the chamber. This analysis is presented in a later section of this thesis.

C. OPTICAL SYSTEM

Illumination of the cloud chamber was accomplished by two (2) alternate means, a flash system and a visual system.

The flash system consisted of two (2) flash tubes 64-in. long mounted on opposite ends of the chamber and backed by metallic parabolic reflectors. The high voltage power supply was connected to a bank of forty 100-microfarad condensers. Ten (10) condensers were maintained at +2000 volts and ten (10) at -2000 volts and were connected permanently across a flash tube. A similar system was employed independently for a second flash tube. Arcing of the tubes, thus discharge of the condenser banks, was accomplished by means of an induction, or tickler, coil which in turn received its pulse from the control chassis.

The visual system consisted of eight (8) movie projection bulbs, four (4) on each side of the chamber. This second system was necessitated by the inability to look at the high intensity flash of the first system. Visual inspection was mandatory for the purpose of setting the expansion ratio of the chamber.

Selection between the alternate lighting systems was made via the auxiliary control panel. A drive motor rotated each set of lights through 180 degrees into the focal point of the paraboloid on appropriate switching. The flash tubes, of course, were normally left at those focal points during automatic chamber operation and photographing.

Photographs were taken in stereoscopic view by means of two (2) specially built cameras which were located at a distance of 660.4

centimeters from the center of the chamber. The stereoscopic cameras shown in figure 6, page 20, were separated by a distance of 93.98 centimeters. The cameras were equipped with two (2) Eastman Kodak Ektanon 10-in. lenses. The normal setting for the lenses was f/16. The film used was Eastman 70-millimeter Linagraph Panchromatic film. Approximately five hundred (500) pictures were taken per 100-ft roll.

D. TARGETS

Two types of targets were used during the period of the experiment, internal and external.

The internal target consisted of eleven (11) steel plates on the average 2.92 centimeters in thickness. For structural reasons steel was chosen as a target and absorbing material. Ideally a higher density material would have been desirable as an absorber but machining of a substance such as tungsten, or support of a substance such as lead eliminated these more commonly used absorbers. The reflectivity problem also influenced the decision in favor of the steel. Since the mean distance between the plates was about 4 in., the plates were tilted at appropriate angles so as to present an edgewise view to the conical field of the camera lenses.

The desire for a target material of low atomic number led to the consideration of an additional external lithium hydride target. An external water target was tried with only marginal success. A compromise external target of carbon was decided upon and was in place during

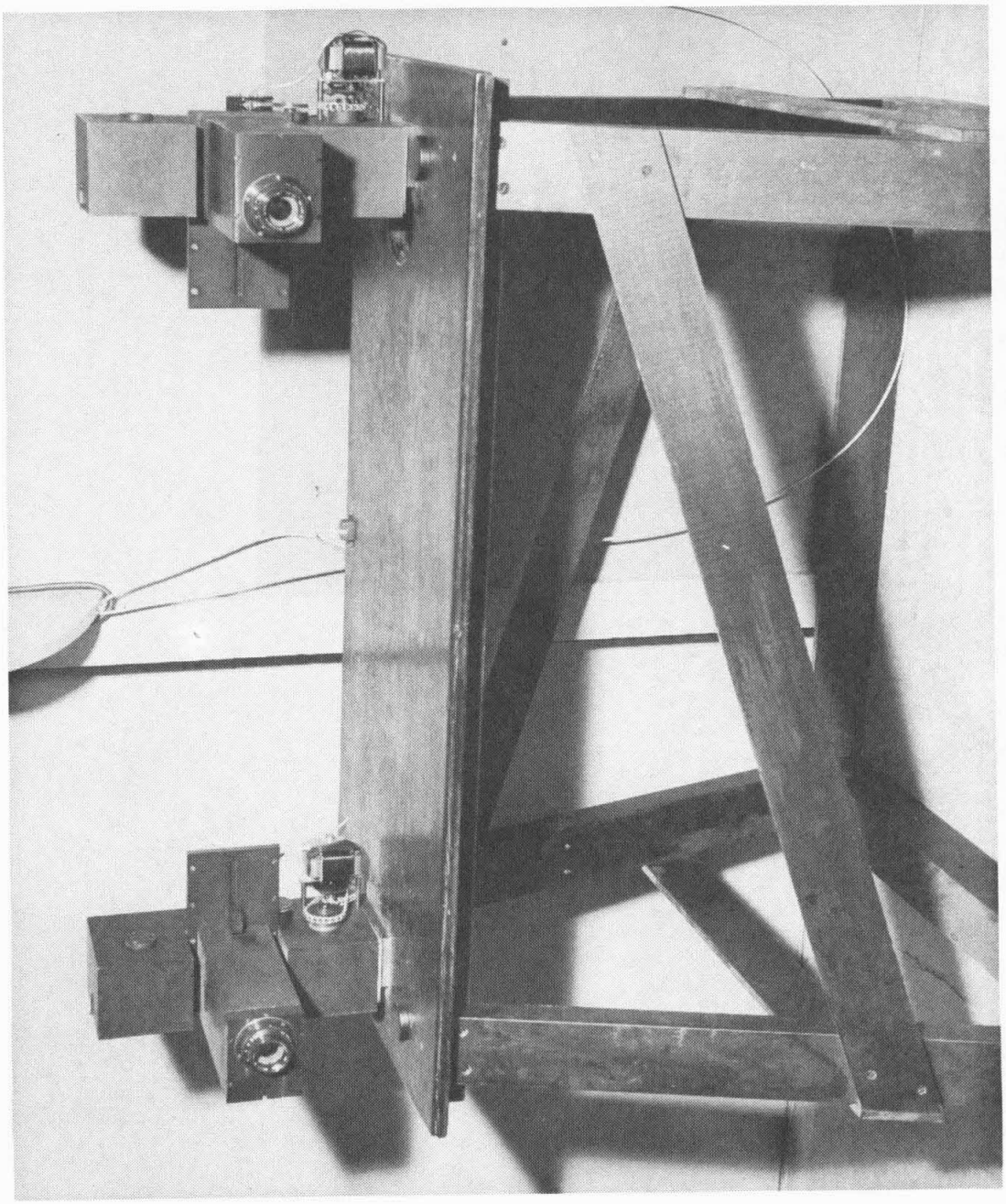

Figure 6. Stereoscopic Cameras

the majority of running time for the instrumentation. The geometric arrangement of the carbon in relation to the geiger tubes and steel plates may be seen in figure 2, page 6. The water target when used was placed on top of the building approximately 7 ft above the chamber.

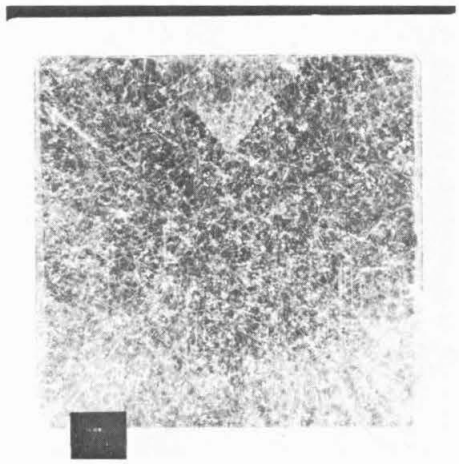

Figure 7a
First Numbered Picture

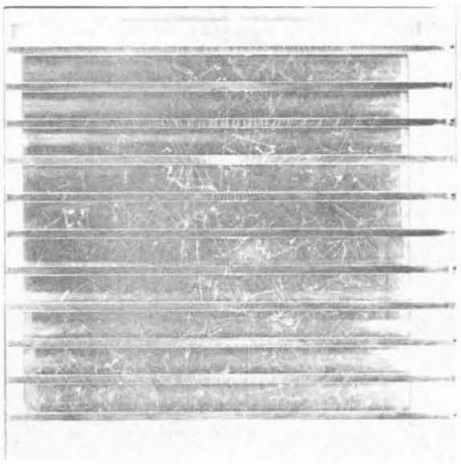

Figure 7b
First Multiplate Picture

Figure 7c
Excessive Condensation

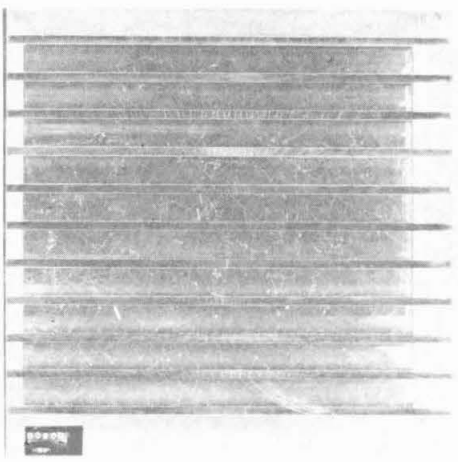

Figure 7d
Effective Beginning of Operation
with Multiplates Installed

Figure 7. Milestones in Chamber Operation

III. THEORY OF HIGH ENERGY INTERACTIONS

The two types of showers observed in the chamber were: (A) Photon-electron Cascades, and (B) Nuclear Cascades.

A. PHOTON-ELECTRON CASCADES

Longitudinal development of photon-electron cascades was carried out by Carlson and Oppenheimer[3] who set forth a series of diffusion equations for the process which yielded the number of photons and electrons at a given depth for a given incident energy. A second method due to Bhabha and Heitler[4] by analysing successive collisions yielded data at the early stages of development of a shower. A summary of the work of these men and others on the longitudinal development of showers was given by Rossi and Griesen[5].

The results of the cascade theory may be summarized as follows,

(1) Simple cascade theory as set forth by Heitler[6] assumed that the energy losses by bremsstrahlung were equal to that by pair production, and considered only these energy loss processes. This yielded a formula,

$$t_{max} = \ln \frac{E_o}{\epsilon_c}$$

where,

t_{max} = depth to the maximum of the shower given in radiation lengths

E_o = initial energy of the shower

ϵ_c = critical energy for the absorber.

The radiation length is defined as that length in which an electron loses

$1 - e^{-1}$ of its energy by radiation. The critical energy is that energy at which an electron loses as much energy per length by radiation as by ionization.

(2)General cascade theory based on the diffusion equations has been solved for two approximations. Approximation A, as worked out by Landau and Rumer[7] assumed correct energy losses for bremsstrahlung and pair production, but neglected, as did simple cascade theory, the losses due to ionization and the Compton effect. This yielded a formula,

$$t_{max} = \ln\left(\frac{E_o}{E} - n\right)$$

where in addition to the symbols identified above,

E = energy of the electrons such that $\epsilon_c \ll E \ll E_o$

n = 1.0 for an electron initiated shower and 0.5 for a photon initiated shower

Although this solution is complete its utility is limited due to the unknown parameter E contained therein.

(3)The general cascade theory Approximation B assumed the correct energy losses for bremsstrahlung, pair production and ionization but neglected the losses due to the Compton effect. It yielded a formula,

$$t_{max} = \ln\left(\frac{E_o}{\epsilon_c} - n\right)$$

(4)Correspondingly for the simple cascade theory the number of electrons at the maximum was given by,

$$N_{max} = \frac{2E_o}{3\epsilon_c}$$

where in addition to the parameters defined on the preceding page,

N_{max} = number of electrons at the maximum of the shower.

(5) A similar expression under general cascade theory with Approximation A was not useful because it involved the number of electrons greater than the energy E defined on the preceding page.

(6) Under Approximation B of the general cascade theory the expression for the number of particles at the maximum became

$$N_{max} = \frac{0.31}{\left(\ln \frac{E_o}{\epsilon_c}\right)^{1/2}} \frac{E_o}{\epsilon_c}$$

The graphical solution is set forth in many well known references on cosmic rays including Rossi[8], Janossy[9], and others. It is to be noted that a more sensitive criterion in the measurement of the energy of the primary is that of the number of particles at the maximum, N_{max}, rather than the depth to the maximum, t_{max}. These formulae were used in a photometric determination of the energies of pi-zero mesons resulting from nuclear interactions. Since the pi-zeros decayed with a half life of $\sim 10^{-15}$ seconds into two gamma rays, the subsequent development of two photon-electron cascades occurred. Details of this analysis are to be found in a later section of this thesis.

B. NUCLEAR CASCADES

Theoretical work on the production of mesons in nucleon-nucleon collisions has been developed by Heisenberg[10], Lewis et.al.[11], and Fermi[12,13]. Models for high energy nuclear interactions have essen-

tially been based on thermodynamics.

(1) The first endeavor in a meson production theory was undertaken by Heisenberg. The analysis yielded the following formula,

$$N = \frac{W^*}{\mu \ln \frac{W^*}{\mu}}$$

where,

N = number of mesons produced

W^* = total energy of the incident nucleon in the center of mass system

μ = rest mass energy of the produced mesons.

(2) In the theory set forth by Lewis, Oppenheimer, and Wouthuysen[11] a breaking radiation model was used which yielded the following formula,

$$N = 2\left(\frac{W_1}{M_1}\right)^{1/3}$$

where in addition to the symbols identified above,

W_1 = total energy of the primary nucleon in the laboratory system

M_1 = rest mass energy of the primary nucleon.

(3)The Fermi analysis was also a thermodynamic model which yielded

$$N \propto (W_1)^{1/4}$$

$$N \propto (W^*)^{1/2}$$

This proportionality is believed to hold whether N represents the mesons only, or both the nucleons and mesons produced. Belenkii

and Landau[14] have done independent work obtaining the same proportionality. The coefficients of proportionality were calculated by Belenkii and Landau. More recently Hazen, Heineman, and Lennox[15] calculated additional proportionality constants as a function of various impact parameters. A graph of the Fermi formula assuming a proportionality constant of one (1) which is not a great variance with the results of any of the above is shown in figure 8, page 28.

(4) An alternate approach for obtaining the total energy of the primary is set forth in Appendix C, by use of the angle transformation formula developed therein with certain restricted assumptions. The angle transformation for the paths taken by particles as seen from a laboratory and center of mass system is given by,

$$\tan \theta = \frac{\sin \theta^*}{\gamma_c \left(\cos \theta^* + \frac{\beta_c}{\beta^*} \right)}$$

where,

θ = angle measured in the laboratory system from a line along which the relative velocity of the laboratory and center of mass systems takes place,

θ^* = angle measured in the center of mass system from a line along which the relative velocity of the laboratory and center of mass systems takes place,

$$\gamma_c = \frac{1}{\sqrt{1 - \beta_c^2}}$$

MEDIAN ANGLE FORMULA

$$W_1 = \frac{2M_1}{\tan^2\theta}$$

MESON PRODUCTION FORMULA (FERMI)

$$N = \left(\frac{W_1}{M_1}\right)^{1/4}$$

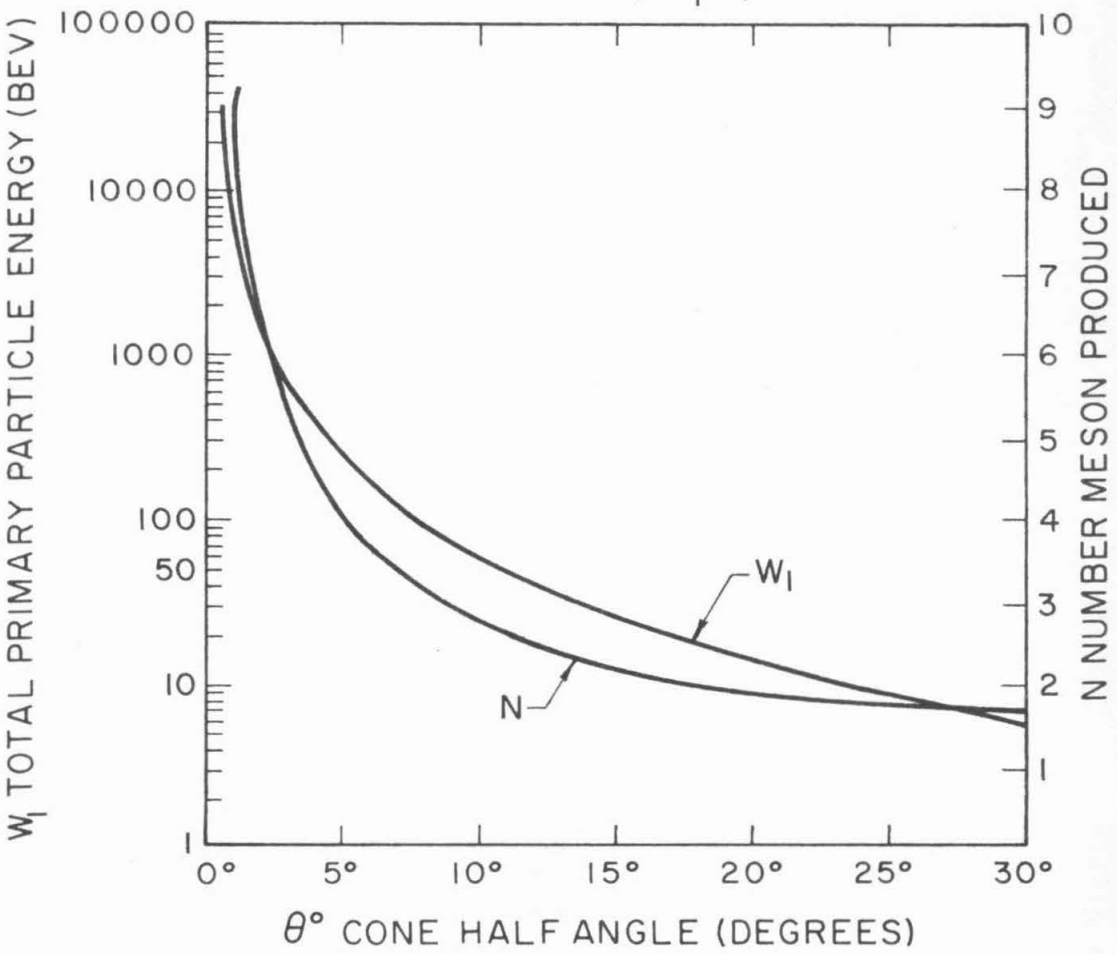

Figure 8. Median Angle Formula and Meson Production Formula

$\beta_c = \frac{v}{c}$ = velocity of the center of mass, as viewed from the laboratory system, divided by the velocity of light,

$\beta^* = \frac{u^*}{c}$ = velocity of a particle in the center of mass system, divided by the velocity of light.

If an incoming particle, say a nucleon, is considered in the laboratory system as traveling with large velocity, the total energy is large compared to its rest mass energy. The angle transformation formula may then be approximated by,

$$\tan \theta = \left(\frac{2M_1}{W_1}\right)^{1/2} \tan \frac{\theta^*}{2}$$

The incoming nucleon upon hitting a target may produce many mesons. If the mesons were emitted isotropically in the center of mass system a single cone would be observed in the forward direction. Actually two cones, a narrow and a diffuse cone, are observed. This can be interpreted as arising from a symmetric double cone of meson emission in the center of mass system. Such a situation is illustrated in figure 9, page 30.

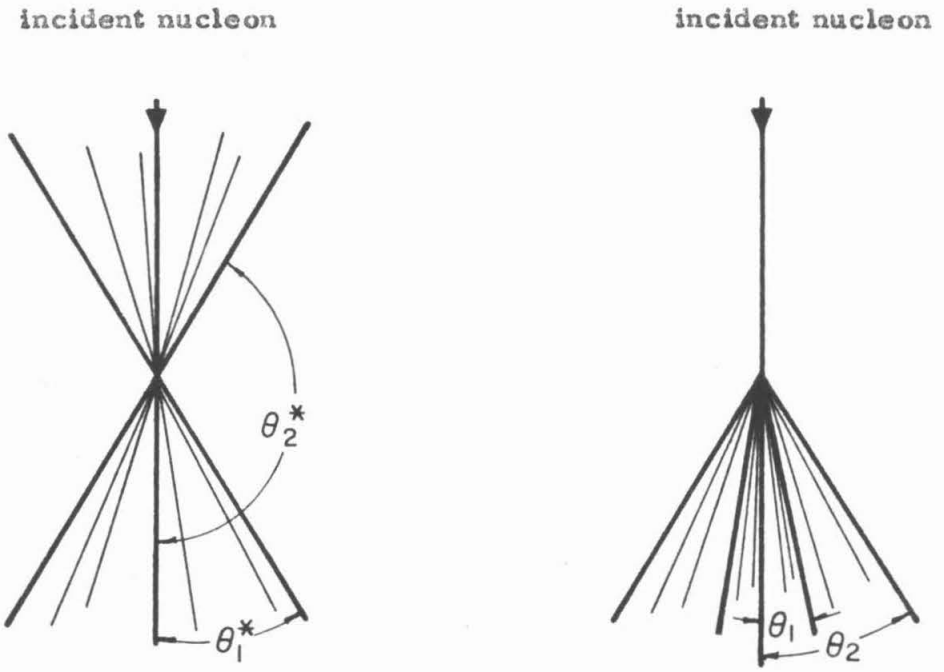

Figure 9. Meson Cones

θ_1^* = angle of the forward cone in the center of mass system.

θ_2^* = angle of the backward cone in the center of mass system.

θ_1 = angle of the narrow cone in the laboratory system (corresponding to the forward cone of the center of mass system).

θ_2 = angle of the diffuse, wide cone in the laboratory system (corresponding to the backward cone of the center of mass system).

Applying the angle transformation formula approximation for incident nucleons of high energy,

$$\tan \theta_1 = \left(\frac{2M_1}{W_1}\right)^{1/2} \tan \frac{\theta_1^*}{2}$$

$$\tan \theta_2 = \left(\frac{2M_1}{W_1}\right)^{1/2} \tan \frac{\theta_2^*}{2}$$

$$= \left(\frac{2M_1}{W_1}\right)^{1/2} \tan \left(\frac{\pi - \theta_1^*}{2}\right)$$

$$= \left(\frac{2M_1}{W_1}\right)^{1/2} \cot \frac{\theta_1^*}{2}$$

$$= \left(\frac{2M_1}{W_1}\right)^{1/2} \frac{1}{\tan \frac{\theta_1^*}{2}}$$

Multiplying the expressions for $\tan \theta_1$ and $\tan \theta_2$

$$W_1 = \frac{2M_1}{\tan \theta_1 \tan \theta_2}$$

thus by measuring the angles of both the narrow and wide cones in the laboratory system the energy of the incoming nucleon can be computed.

A modified means, following the same line of reasoning as above, for determining the energy of the incident nucleon can be obtained by assuming the isotropic distribution of the mesons in the center of mass system. The median angle formula is thus obtained and given as follows,

$$W_1 = \frac{2M_1}{\tan^2 \theta}$$

where the symbols are as identified on the preceding page except that,

θ = the half angle of the cone in the laboratory system which contains one half the particles produced.

This formula was used extensively in making primary energy estimates of nuclear showers and is shown graphically in figure 8, page 28.

(5) Yet another approach for attaining the total energy of the primary is set forth in Appendix F. The method is based on taking logarithms of the angle transformation formula, and yielded the following result

$$\ln \gamma_c = - \frac{1}{n} \sum_{i=1}^{n} \ln \left| \tan \theta_i \right| \pm \frac{\sigma}{\sqrt{n}}$$

where in addition to the symbols identified above,

n = the number of particles emanating from a nuclear interaction,

θ_i = the angle of the i-th particle measured with respect to the line of flight of the primary particle,

σ = the standard deviation.

This equation is based on the assumption of the symmetric distribution of angles with respect to the equatorial plane, and that neither the angles, nor the energies of emission of the particles are correlated. The formula was used in making estimates of the energies of the small interactions.

IV . SIGNIFICANT PARAMETERS FOR THE CLOUD CHAMBER

Significant parameters in the chamber operation necessary for data reduction were (A) Radiation Length, (B) Critical Energy, (C) 50 Bev Photon-electron Cascade, (D) Cross Section, and (E) Mean Free Path.

A. RADIATION LENGTH

A unit radiation length, X_o , is defined by the formula

$$\frac{1}{X_o} = 4\alpha\frac{N}{A} Z(Z+1) r_e^2 \ln(183 Z^{-1/3})$$

where

α = the fine structure constant

$= \frac{e^2}{\hbar c}$ in c.g.s. e.s.u.

$= \frac{e^2}{4\pi\epsilon_o \hbar c}$ in rationalized m.k.s.a.

$= \frac{1}{137.0377}$

e = the charge on the electron

$\hbar$ = Planck's constant divided by 2π

c = the velocity of light

ϵ_o = the permittivity of free space

N = Avogadro's number

A = the atomic weight of the absorber

Z = the atomic number of the absorber

r_e = the classical radius of the electron

$= \frac{e^2}{mc^2}$ in c.g.s. e.s.u.

$$= \frac{e^2}{4\pi\epsilon_o mc^2} \text{ in rationalized m.k.s.a.}$$

$$= 2.81784 \times 10^{-15} \text{ meters}$$

m = the rest mass of the electron.

As pointed out previously a radiation length is defined as that length where the electron drops to $\frac{1}{e}$ of its original energy.

Such a definition is convenient since for electrons which bremsstrahlung, the energy loss, per gram per square centimeter of absorber divided by the energy of the radiating electron is given by

$$4\alpha \frac{N}{A} Z(Z+1) r_e^2 \left[\ln(183 Z^{-1/3}) + \frac{1}{18} \right].$$

Similarly the probability that a photon will produce an electron pair per gram per square centimeter may be written as

$$4\alpha \frac{N}{A} Z(Z+1) r_e^2 \left[\frac{7}{9} \ln(183 Z^{-1/3}) - \frac{1}{54} \right].$$

For the steel plates of the chamber,

X_o = 14.1 grams/(centimeter)^2/radiation length

Since the density of the steel, ρ , is given by

ρ = 7.91 grams/(centimeter)^3,

and the thickness/plate, d , was

d = 2.92 centimeters/plate,

the number of grams/(centimeter)^2/plate, ρ d,

ρd = 23.1 grams/(centimeter)^2/plate.

Thus the absorbing thickness for each plate, t , may be given in radiation on lengths as

$$t = \frac{\rho d}{X_o}$$

$$= 1.64 \text{ radiation lengths/plate.}$$

Since the number of plates in the chamber, n , was

$$n = 11 ,$$

the total number of radiation lengths, t_{total} , in the chamber was

$$t_{total} = nt$$

$$= 18.0 \text{ radiation lengths/chamber}$$

The total number grams/(centimeter)^2/chamber, $\rho\, d_{total}$, was

$$\rho\, d_{total} = n\, \rho\, d$$

$$= n\, X_o t$$

$$= X_o t_{total}$$

$$= 254 \text{ grams/(centimeter)}^2\text{/chamber.}$$

B. CRITICAL ENERGY

As previously pointed out the critical energy is defined as that energy at which an electron loses as much energy per length by radiation as by ionization. The critical energy, ϵ_c , is given approximately by

$$\epsilon_c = \frac{750}{Z} \text{ Mev}$$

where

Z = the atomic number of the absorber.

The value is given more accurately by Rossi[8] for iron as

$$\epsilon_c = 24.3 \text{ Mev.}$$

C. 50 BEV PHOTON-ELECTRON CASCADE

On the basis of simple cascade theory utilizing the parameter of the previous section, the depth, t_{max}, for a 50 Bev photon-electron cascade may be calculated.

$$t_{max} = \ln \frac{E_o}{\epsilon_c}$$

$$= 7.62 \text{ radiation lengths}$$

$$\frac{t_{max}}{t} = 4.64 \text{ plates}$$

On the basis of the graph given in Rossi[8] for Approximation B of the general cascade theory there is agreement with this numerical value.

The number of particles, N_{max}, at the maximum of a 50 Bev photon-electron cascade on the basis of simple cascade theory, yields a result which is too high, because of the approximate nature of that theory. The graphical solution of Approximation B of the general cascade theory is given in Rossi[8]

$$N_{max} = \log_{10} 2.3 \text{ to } \log_{10} 2.4$$

$$= 200 \text{ to } 250 \text{ particles.}$$

This result is in agreement with the numerical solution to Approximation B given by

$$N_{max} = \frac{0.31 \frac{E_o}{\epsilon_c}}{\left(\ln \frac{E_o}{\epsilon_c}\right)^{1/2}}$$

$$= 232 \text{ particles.}$$

These results were utilized as lower limit selection criteria for pi-zero decays initiating photon-electron cascades in nuclear interactions.

D. GEOMETRIC CROSS SECTION

The geometric cross section, σ_g, is given by

$$\sigma_g = r_n^2$$

$$= \pi r_o^2 A^{2/3}$$

where,

r_n = the radius of the nucleus

r_o = the radius of a nucleon

A = the atomic weight.

Therefore, for the iron nuclei of the chamber

$$\sigma_g = \pi (1.41 \times 10^{-13})^2 (55.8)^{2/3}$$

$$= 910 \times 10^{-27} (\text{centimeter})^2$$

$$= 910 \text{ millibarns.}$$

For a nucleon the geometric cross section, σ, is given by

$$\sigma = \pi r_o^2$$

$$= 62.5 \text{ millibarns.}$$

E. GEOMETRIC MEAN FREE PATH

The geometric mean free path is given by Rossi[8] as

$$L_g = \frac{A}{N \sigma_g}$$

where in addition to the symbols identified above

L_g = the geometric mean free path

$$L_g = \frac{55.8}{6.02 \times 10^{23} \times 910 \times 10^{-27}}$$

$$= 102 \text{ grams/(centimeters)}^2 .$$

In terms of radiation lengths the geometric mean free path is given by

$$t_g = \frac{L_g}{X_o}$$

where

t_g = the geometric mean free path in radiation lengths.

$$t_g = \frac{102}{14.1}$$

= 7.23 radiation lengths.

$$\frac{t_g}{t} = \frac{7.23}{1.64}$$

= 4.42 plates.

V. PHOTOELECTRIC SCANNER

A photoelectric scanner was developed as a particle counter for photon-electron cascades.

A. INSTRUMENTATION FOR PHOTOMETRIC TECHNIQUE

Since the number of particles at the maximum of a photon-electron cascade is a more sensitive criterion than the depth to the maximum, an endeavor was made to develop a means of particle counting photometrically. It is to be noted that the more than 200 particles at the maximum of a 50 Bev cascade rendered direct counting impractical. The instrumentation first considered was a standard micro-photometer. Individual traces made with such a device proved the feasibility of the technique but also made manifest the impracticability of endeavoring to use a device in which the point of scanning was not visible to the operator. Since the cascade tracks emanated radially from a point, the longitudinal scanning of the commercial micro-photometer unnecessarily complicated the geometry.

The stereoscopic projectors used in conjunction with the eighteen (18) inch and forty-eight (48) inch magnets and their associated cloud chambers were tested for uniformity in illumination of the projected image. The condensing lens system was found to yield more uniformity in the projector which had been used with the cloud chamber photographs of the eighteen (18) inch magnet. Therefore it was decided to employ this projection system.

The projected image was displayed on a horizontal glass top table covered with drafting paper. The image was projected from below by means of a lens and mirror system. Adjustment of the magnification was

variable, and was chosen such that the projected image of the distance between two steel plates of the chamber was three quarters (3/4) of an inch. This represented a reduction of five and a third (5-1/3) from the true physical situation. The use of this magnification was dictated by the diameter of the housing of the photocell.

The photocell used was a Dumont 6292 photomultiplier. It was mounted vertically with photosurface down onto the projected image on the table. The device is pictured in figure 10, page 41. A synchronous drive motor and back lash gear mechanism rotated the photocell slowly at a uniform angular velocity.

The base of the photocell was covered by a brass cap with an adjustable width radial slit. Scanning apertures as shown in figure 10 were insertable below the slit and above the table top. The inner scanning aperture had radii of 0.125 and 0.375 inches. The middle scanning aperture had radii of 0.375 and 0.625 inches. The outer scanning aperture had radii of 0.625 and 0.875 inches. Only one aperture was used at a time and it was inserted in a milled groove beneath the phototube so that its center was at the center of rotation. Thus the radial scanning slit on the phototube scanned circumferentially over the annular opening.

The response of the phototube to the opacity of the projected image was amplified by a one stage direct coupled amplifier within the phototube housing. This signal was differenced against a reference voltage obtained from a similar electron tube housed in a separate difference amplifier chassis shown in figure 10. The output of this standard difference amplifier was used to drive either a Varian or a Brown recorder.

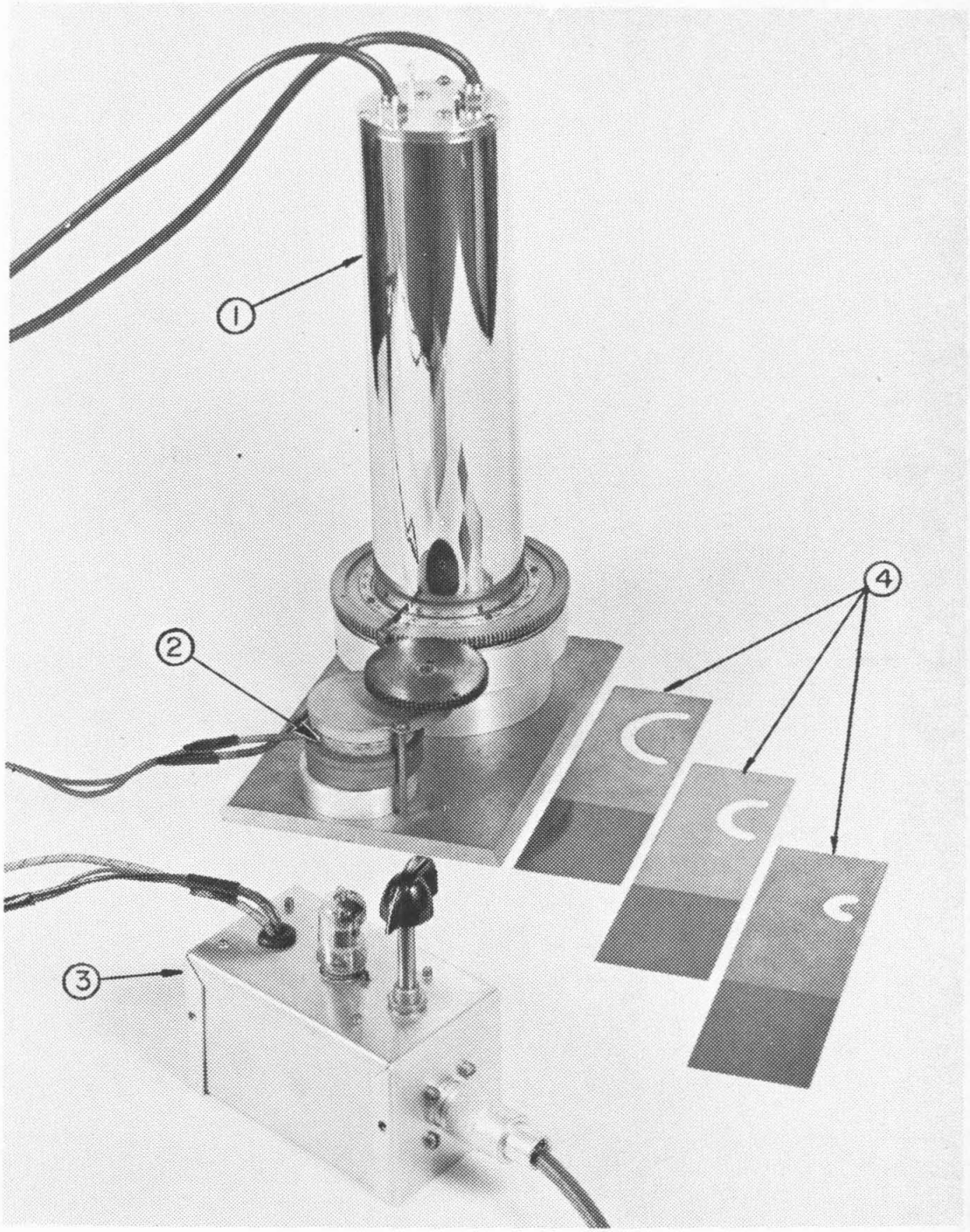

1 Phototube Housing
2 Drive Motor
3 Difference Amplifier
4 Scanning Apertures

Figure 10. Photoelectric Scanner

B. PHOTOMETRIC RESULTS

Typical cascades considered for analysis are shown in figure 11, page 43. Figure 11a shows a small photon-electron cascade. Figure 11b shows two distinct cascades resulting from the decay of a pi-zero meson. As a result of a very energetic collision many pi-zero meson decays are shown in figure 11c. The advent of such cascade processes high in the atmosphere are shown in the extensive air shower of figure 11d.

The endeavor of the photometric analysis was to count the number of particles at the maximum of a photon-electron shower. Typical of the traces obtained are those shown in figure 12, page 44. The traces were taken with the three scanning apertures described in the preceding section. It will be noted that resolution of individual tracks was not possible on the inner aperture wherein three major peaks are discernible. On the outer aperture of figure 12, however, all seventeen (17) tracks are countable, even though some do not fully satisfy the Rayleigh criterion for resolution. It should be noted by extending a horizontal line between the minima of the curves that for an individual scan the variation in white level is not more than about 3% of the total variation from dark level to white level.

The difference from dark level to white level of the center scan is noted to be about 20% greater than either the inner or outer scan. These foregoing variations were primarily attributable to the non-uniformity of the light in the projector. A fraction of this variation not in excess of 5% was determined experimentally to be attributable to non-uniform illumination in the cloud chamber. By use of a diffusing screen in the optical condensing system of the projector the overall variation from dark level

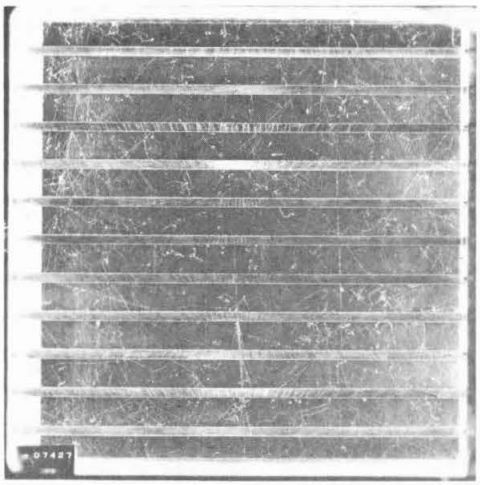

Figure 11a
Photon-Electron Cascade

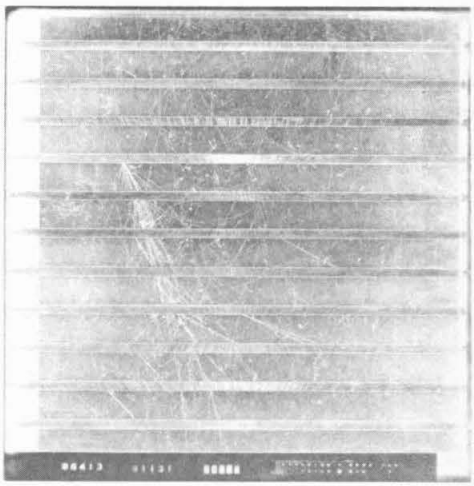

Figure 11b
Two Distinct Cascades Resulting
from Pi-Zero Meson Decay

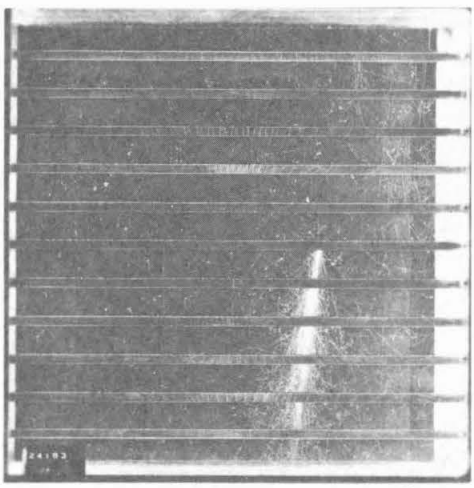

Figure 11c
Superimposed Cascades
Resulting from Many
Pi-Zero Meson Decays

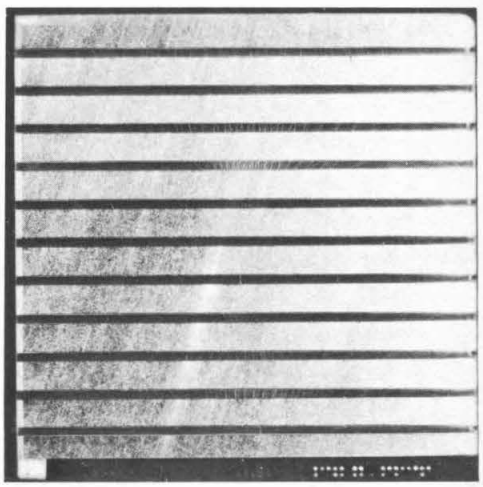

Figure 11d
Photon-Electron Cascades
in Air Shower

Figure 11. Typical Cascades

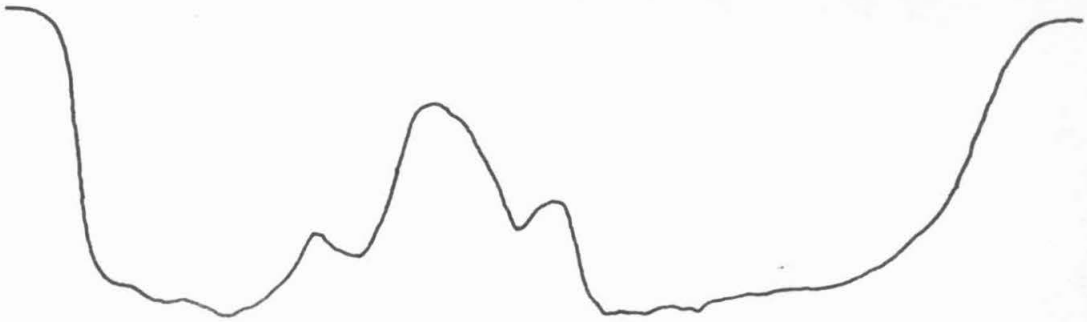

Figure 12a Inner Scanner Aperture

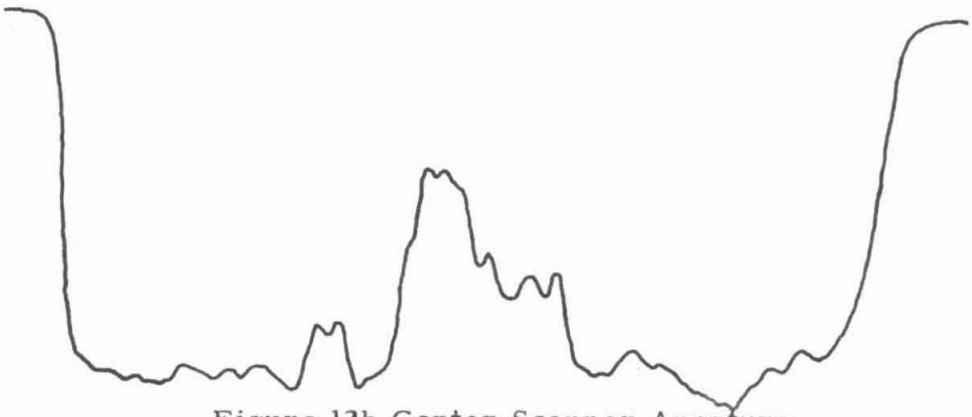

Figure 12b Center Scanner Aperture

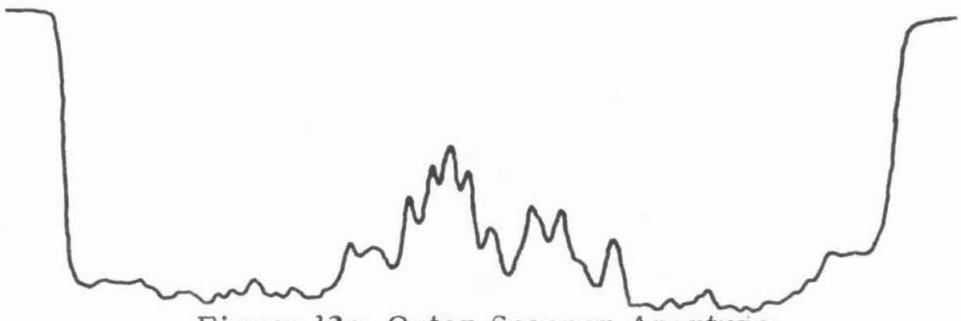

Figure 12c Outer Scanner Aperture

Figure 12. Photometric Traces

to white level for different scanning apertures was reduced to about 10%.

In the photon-electron cascade photometric traces, figure 12, page 44, superposition of the tracks even on the inner scanning aperture was not of sufficient intensity to saturate the photographic emulsion. This was determined by the use of a planimeter and also independently by counting of squares underneath the curves of the recorder traces. The major precaution in both these techniques was to determine the cut off point or white level. As pointed out above the white level was not of equal intensity on both sides of the photon-electron cascade peaks. Judgement, therefore, had to be exercised in determining the cut off points, by a visual comparison with the projected image. In particular the outer scanning aperture trace was counted as having 340 squares beneath the curve. The center scanning aperture trace was counted as having 420 squares beneath the curve. The numbers were in the ratio of their respective dark level to white level differences.

To circumvent the problem of the difference in dark level to white level between scanning apertures a minimum ionizing comparison track was utilized for each scanning aperture independently. Additional caution had to be exercised to guarantee that all tracks were of the same ionization. This presented no problem in the case of photon-electron cascades but was a major concern in nuclear cascades with photon-electron components resulting from pi-zero decay. The problem of the intrusion of the tracks of heavily ionizing nucleons and pions was never completely solved. Clearly it was necessary to exclude these tracks, however, the superposition of the tracks resulted in traces which did not return to white level com -

pletely. Thus only crude estimates could be made of the contaminating contribution of the heavy tracks.

The photon-electron cascade of figure 11a, page 43, containing seven (7) tracks at the maximum was used extensively in calibration work. With it the essential linearity of the photometric technique was established.

Figure 11b, page 43, contained two distinct photon-electron cascades resulting from a pi-zero decay. The cascades were separated by an angle of 11°. Since these cascades were of about the same energy, application of the formula for equal energy gamma rays contained in Appendix D yielded an energy of 1.40 Bev. Both photometric and visual counts at the maxima of the two cascades yielded 40 particles which corresponded to an energy of 1.46 Bev. Since the two maxima occurred at the same depth the principle of superposition could be invoked to use the formulae of simple theory as set forth in Section III. The modulation of this linear proportionality between the number of particles at the maximum, N_{max}, and the energy of the shower, E_o, by the factor $(\ln E_o / \epsilon_c)^{-1/2}$ given by general cascade theory was ignored.

When many pi-zero mesons decayed as shown in figure 11c, page 43, difficulty in analysis arose due to what might be termed a geometric shape factor. Obviously the gamma rays were not all of equal energy. Thus the distance to the maximum of the photon-electron cascade for each gamma ray was different. Even barring the modulation factor given above, uncertainty was introduced by the technique because of the energy distribution of the gamma rays. If one were to assume all gamma rays were of equal energy, linear superposition could be invoked, but for the general case,

particularly where small numbers of cascades are superimposed, this assumption would not be valid. Photon-electron cascades resulting from many pi-zero decays such as shown in figure IIc, were all shorter and fatter than predicted by cascade theory for initiation by a single photon or electron. Some such cascades were relatively fatter near the top, some near the bottom, thus giving evidence for the statistical variation in pi-zero meson energies. The problem of this geometric shape factor was not solved and represents a major limitation on the photometric technique.

Were some realistic estimate of the energy distribution made, the photometric technique could be used as a future research tool to determine the number of pi-zero mesons resulting from a nuclear collision. The various theories of meson production discussed in Section III could thus be subject to test.

VI. GEIGER COUNTER TRIGGERING ANALYSIS

An analysis was undertaken to establish possible geiger counter triggering bias. An investigation was made of the triggering of the cloud chamber as a function of the (A) Interaction Location and the (B) Primary Particle Energy.

At frame 99,151 a change was made in the use of the hodoscope, which was described in Section II. The geiger counters used in triggering the cloud chamber were connected to the visual display of the hodoscope. The two upper rows of eight(8) hodoscope lights were connected in parallel to the upper of the two geiger counter trays. The two bottom rows of eight (8) hodoscope lights were connected in parallel to the bottom geiger counter tray. The purpose of the parallel connection was to provide a redundancy in the visual display since occasional failure had occurred in the hodoscope due to the critical matching of the tubes and neon bulbs in the various channels. This redundancy proved unnecessary except for two cases. In those cases the larger number of lights illuminated was taken as the number of geiger counters fired. The lights displayed from right to left corresponded to the geiger counters fired from front to back in a tray as seen from the vantage point of the cameras. Both the upper and lower geiger counter trays were below the cloud chamber.

A. INTERACTION LOCATION

Geiger counters had been removed from above the cloud chamber at frame 48,090 in order to eliminate possible triggering bias against neutrons and in favor of protons. This removal, however, did not relieve the

possibility of triggering bias as a function of location of a nuclear interaction within the chamber. Therefore, an investigation was made of this possibility.

The chamber was divided into four parts: 0 - 52 grams/(centimeter)^2, 52^+-104 grams/(centimeter)^2, 104^+-156 grams/(centimeter)^2, and 156^+-208 grams/(centimeter)^2. The latter number was taken as the gate length for this investigation. The number of nuclear interactions in excess of 50 Bev for each of these four (4) parts was plotted versus the total number of geiger counters fired. The minimum number of geiger counters fired for an interaction of this energy was never less than eleven (11).

The data of this investigation is shown in the histograms of figure 13, page 50. The data was also normalized for an equal number of cases in each of the four parts (not illustrated). Inspection of figure 13 reveals no apparent bias in triggering for location of events at the bottom of the chamber. The fifteen (15) cases in the third quarter firing sixteen (16) counters does not appear to be statistically significant.

As a further check the same data plotted by halves i.e., 0 -104 grams/(centimeter)^2 and 104^+-208 grams/(centimeter)^2 was plotted and is shown in figure 14, page 51. Confirmation of the conclusion of a lack of significant bias is again displayed for the two hundred twenty three (223) nuclear interactions which were tabulated.

B. PRIMARY PARTICLE ENERGY

Since those data were already tabulated as a part of the general nuclear interaction analysis, an additional series of plots was made of the

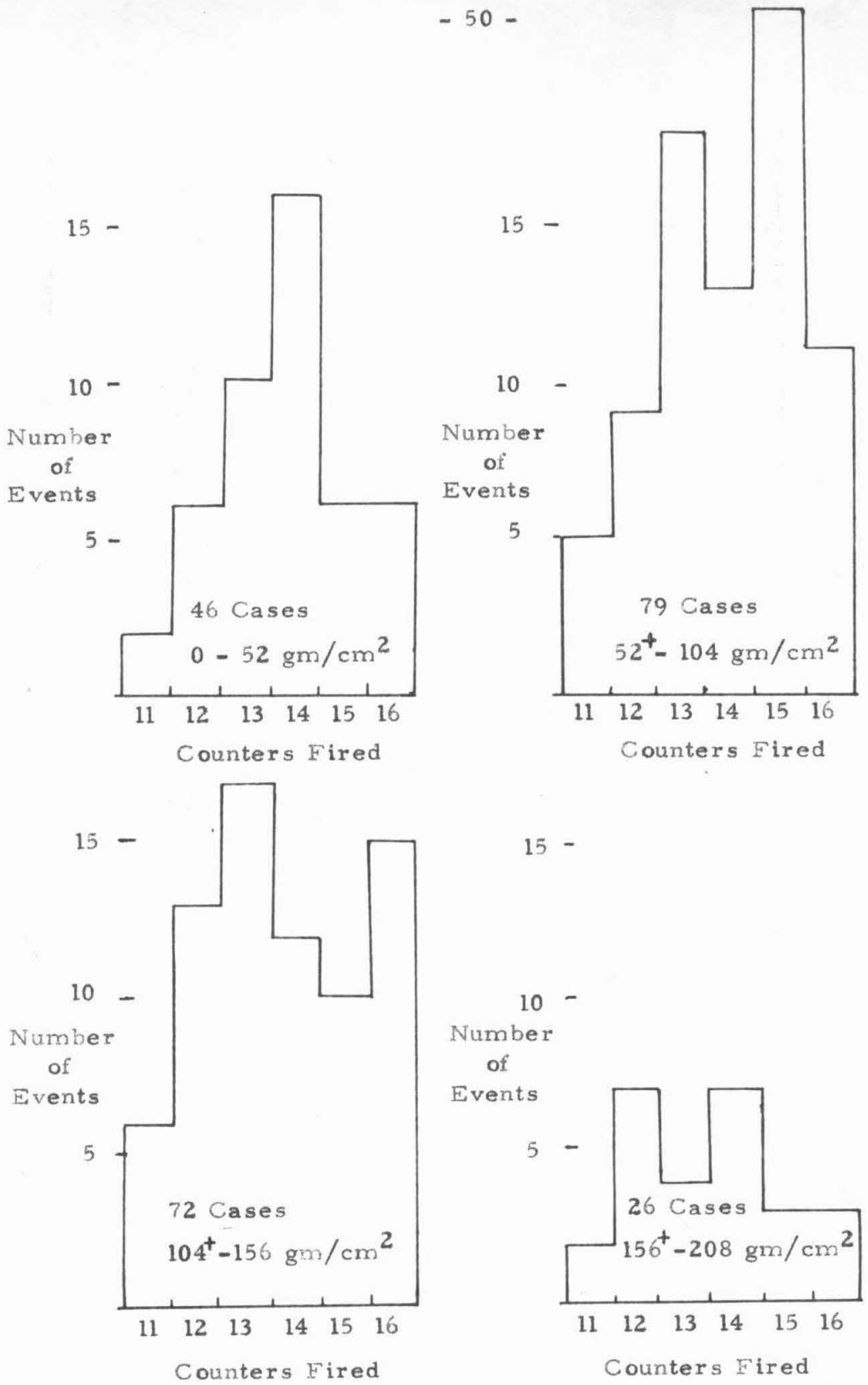

Figure 13. Interaction Location by Quarters as a Function of Triggering

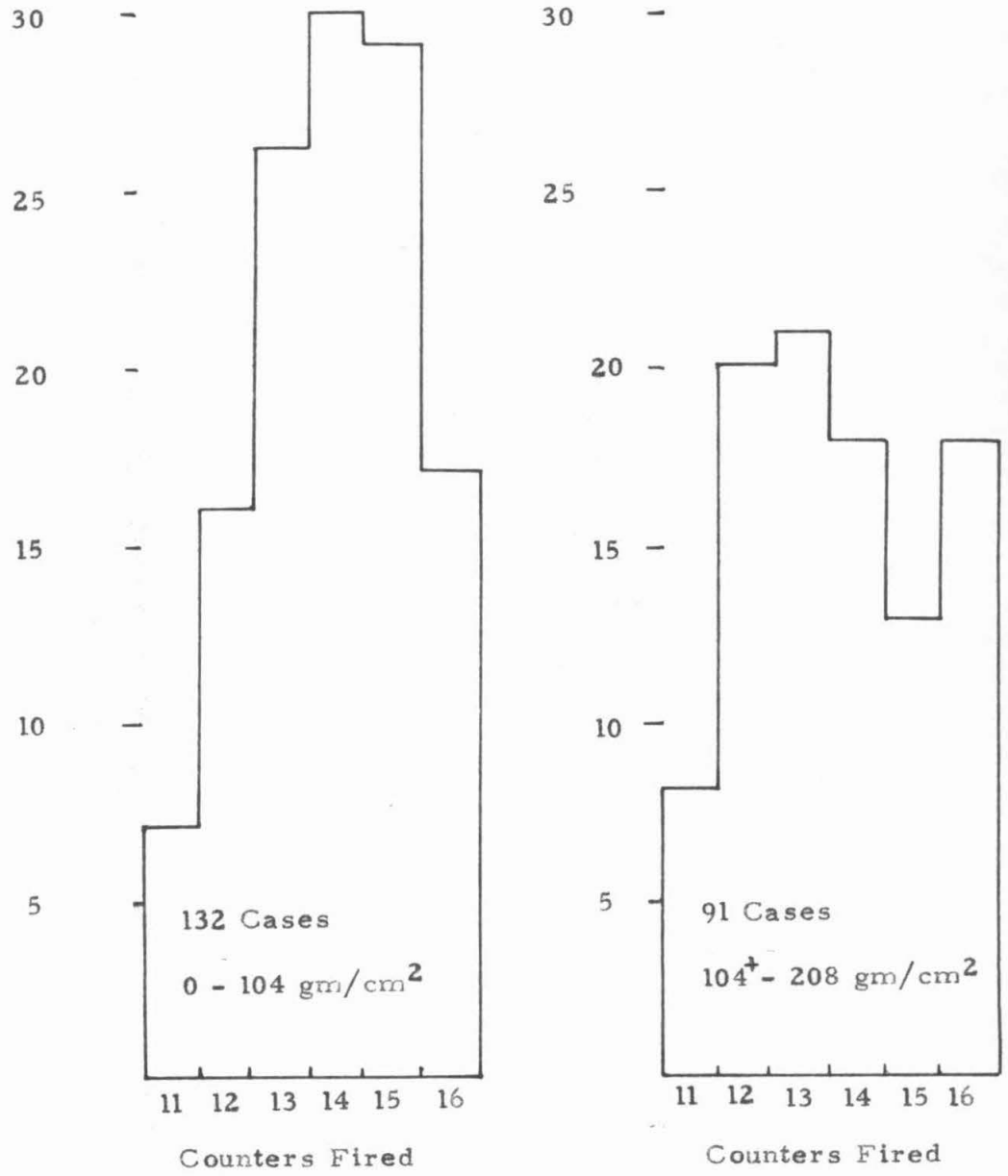

Figure 14. Interaction Location by Halves as a Function of Triggering

number of nuclear interactions of a given primary energy versus the number of geiger counters fired. For this purpose the median angle formula was used to estimate the primary particle energy. The same two hundred twenty three (223) cases were tabulated. Energies were divided into the following catagories: 50 Bev, 100 Bev, 200 Bev, 300 Bev, 400-500 Bev, and 800 Bev and above. The latter two collective groupings were used (1) to obtain a statistically significant number of cases in those groupings approximately equal to the number of cases to each of the first four groupings; and (2) to eliminate part of the uncertainty of estimating high energy events since the cone angle was narrow. Histograms of these six (6) energy divisions are shown in figures 15 and 16, pages 53 and 54 respectively. As can be seen, and would be expected, the higher energy events triggered more counters. The discrepancy to this conclusion would appear to be the 400-500 Bev cases. It is difficult to explain this exception to the general rule except in terms of weak statistics.

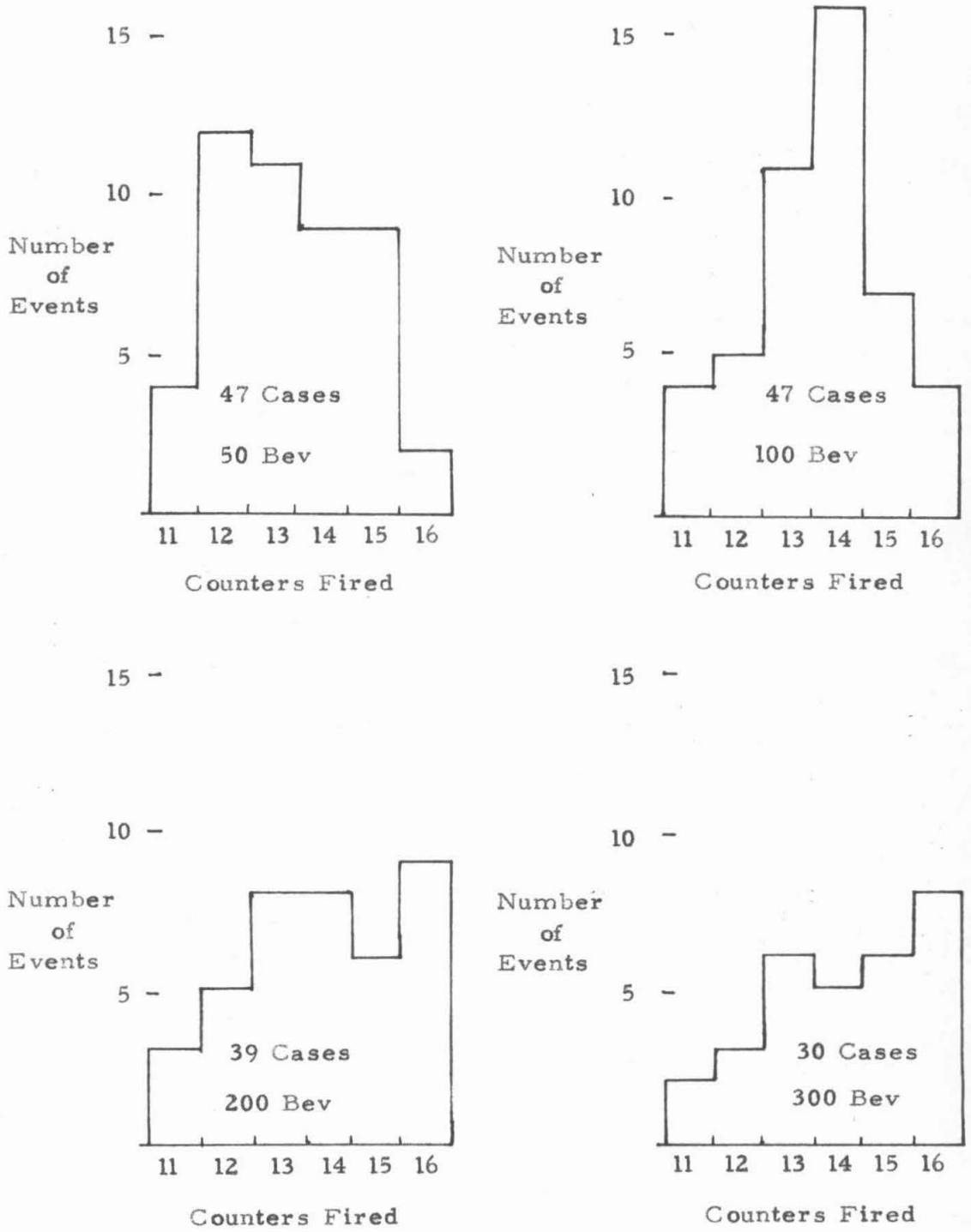

Figure 15. Primary Energies as a Function of Triggering

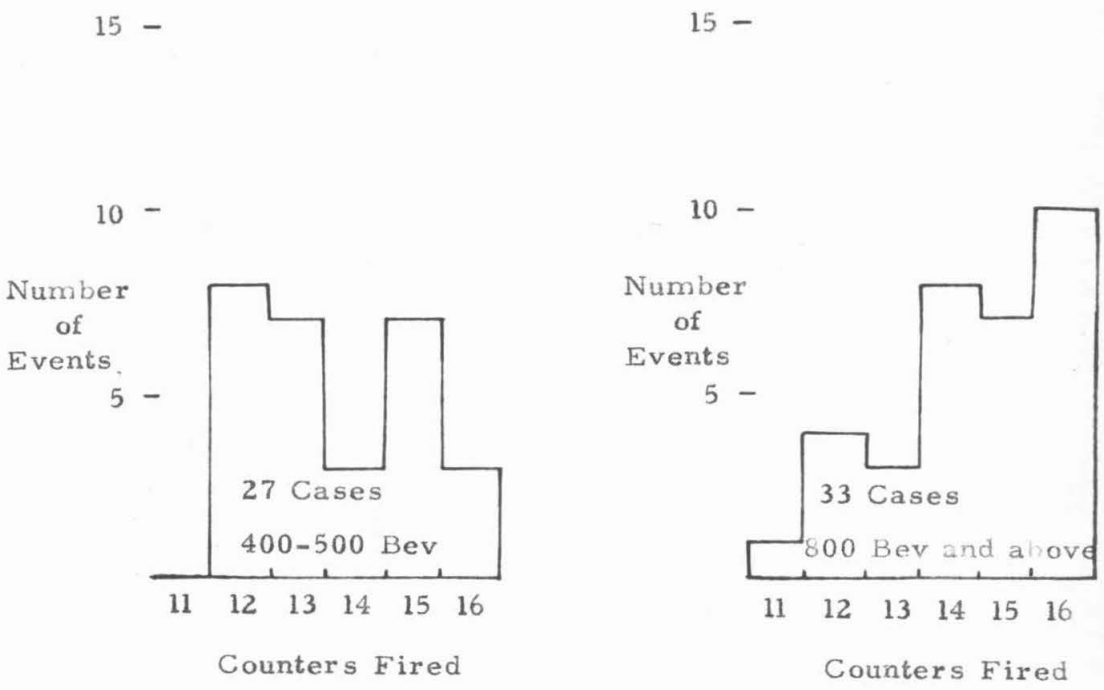

Figure 16. Primary Energies as a Function of Triggering

VII. DOUBLE NUCLEAR INTERACTION ANALYSIS

The film was visually scanned with a stereoscopic viewer for nuclear interactions. Once a large, i.e., energetic, nuclear interaction had been discerned, particular acuity was exercised in the search for a small, i.e., less energetic, nuclear interaction above the large interaction. A typical double nuclear interaction is shown in figure 17, page 56.

A. SELECTION CRITERIA

In selecting the cloud chamber events for analysis three factors were of importance in establishing the acceptability:

(1) Collimation of the event to the vertical,

(2) The nuclear nature of the event,

(3) An energy for the event in excess of 50 Bev.

The first factor caused events to be selected which were of near constant gate length. This aided the data analysis, since only a small correction to the path length through the steel plates of the chamber had to be made. Events photographed during the early operation of the chamber were well collimated to the vertical by the nature of the geiger counter coincidence arrangement, since at least one geiger counter in the array above the chamber had to be fired in coincidence with several geiger counters in two banks below the chamber. In the later operation of the chamber, from which the data was selected for analysis in this thesis, events were not as well collimated since the upper geiger counter tray was removed. The selection criterion established for collimation during the visual scanning was the following:

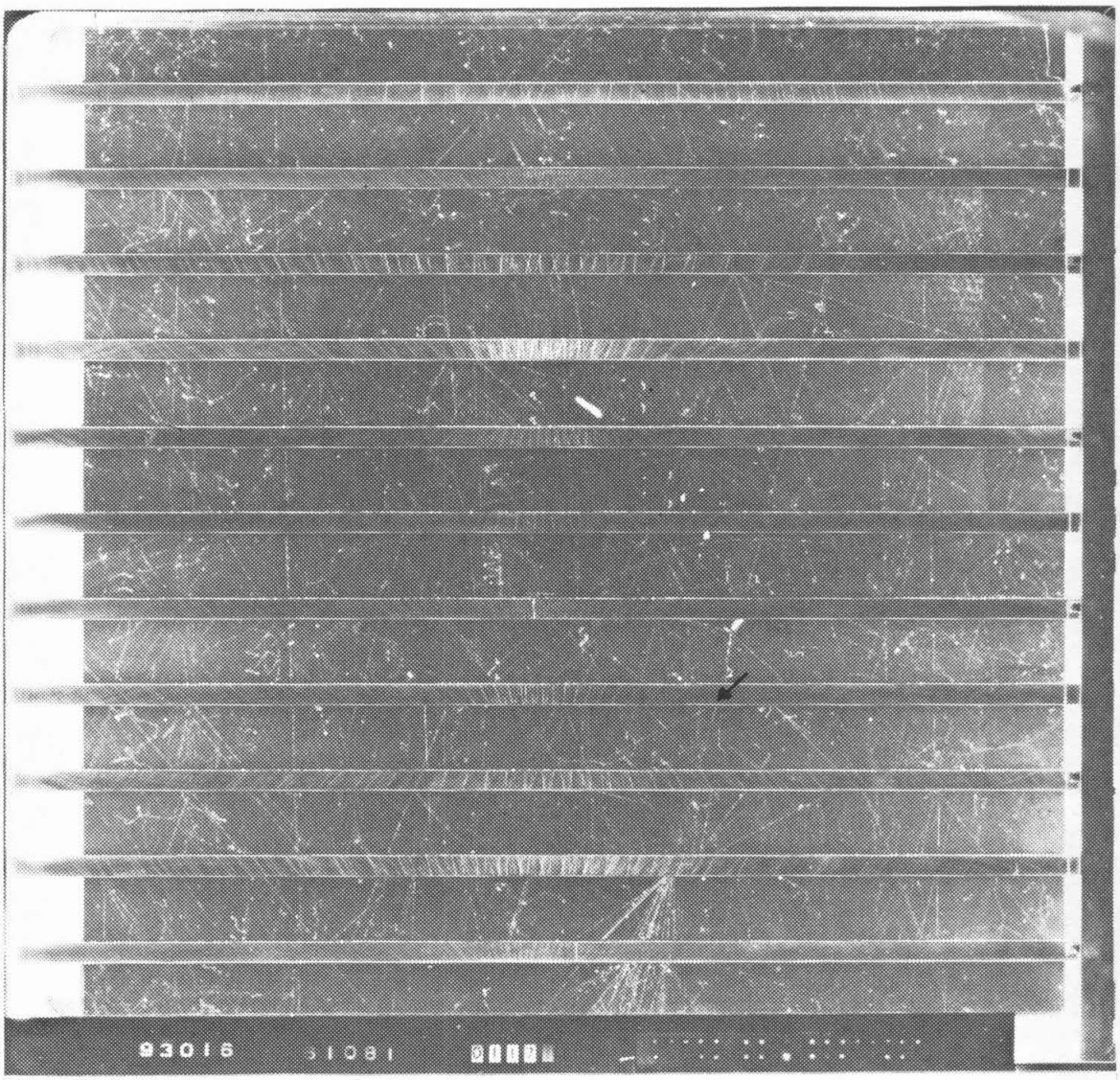

Figure 17. Double Nuclear Interaction
(Charged - Charged)

(1) The projected line of flight of the incident particle which caused nuclear interaction had to cross both the top and bottom steel plate in the chamber within the 58 inch by 22 inch area of the plate.

The second factor, that of the nuclear nature of the event, was partially established by the elimination of events occurring in the first plate. Photon-electron cascades resulting from gamma rays produced from above the chamber were eliminated, since as calculated in Section IV, there were 1.64 radiation lengths/plate. Elimination of events in plate one also permitted observation of the incident particle track through two 4 inch spaces for an easier establishment of the first criterion. The presence of penetrating particles emanating from the point of interaction also established the nuclear nature. The plate thickness made it improbable that electrons or photons would pass through a plate without interaction. The penetrating particles were therefore most likely pi-mesons or nucleons. Although many showers were mixed, containing both photon-electron cascades and penetrating particles, if penetrating particles were present the shower was established as nuclear. The photon-electron component was interpreted as resulting from the decay of pi-zero mesons. The selection criteria for establishing the nuclear nature of the interaction were:

(2a) Interactions occurring in the first plate were excluded. This criterion established the bottom of the first plate as the upper fiducial reference.

(2b) The presence of one or more penetrating particles emanating from the point of interaction was required.

If a shower were of a photon-electron nature only, as was pointed out in Section IV, 4.64 plates would be necessary to establish that it was of 50 Bev or greater, if one were to use the depth to the maximum as a criterion. With penetrating particles present this many plates was not necessary, since the penetrating particles carried away part of the energy. Additionally by observing the cone angle of the mesons and nucleons coming from the interaction one could establish the energy by employing the median angle formula discussed in Section III. The following criteria were set forth for establishing 50 Bev as a lower limit to the large nuclear interaction:

(3a) Interactions occurring in the last plate were excluded. This permitted the last two spaces to be used to observe the shower development. This criterion also established the bottom of plate ten as a lower fiducial reference.

(3b) The median angle formula as graphed in figure 8, page 28 was used to establish the lower limit of energy selected.

If a double interaction occurred in which the large interaction satisfied the above criteria but the small interaction did not, as was the case for two events in which the small interaction occurred in plate one, the

interaction was regarded as a single interaction.

Additional restrictive criteria establishing the nature of the small interaction were required. In conjunction with the collimation problem and the inter-relation between the small and large interaction, it was necessary that the two interactions be approximately on the same line of flight. Therefore, the collimation was established by the following criterion:

(4) When a small interaction was found above a large interaction, the line of flight of the particle creating the small interaction had to be within 1° of the line of flight of the particle creating the large interaction.

Many large interactions satisfying the criteria of 1 - 3 above, and for which the small interaction occurred in compliance with criterion 4, could not be regarded as double nuclear interactions since the smaller interaction was not nuclear. These were the usual knock-on electron processes and were excluded. The nuclear nature of the small interaction was established by use of criterion 2b above.

The selection criterion establishing the upper limit of energy of the small interaction will be discussed in a later section.

B. DATA FOR LARGE INTERACTIONS

A total of six hundred thirty-six (636) cases of large interactions with energy in excess of 50 Bev, established in accordance with the above criteria, were tabulated. Energy estimates obtained by the median angle formula were made for each case.

The angles of the line of flight seen on the film in each view were listed as θ_L for the left view, and θ_R for the right view. Appendix E describes the method used in obtaining an approximate formula for the true angle in space, θ_T . The relation derived was

$$\sec^2 \theta_T = 1 + \frac{1}{4}(\tan \theta_L + \tan \theta_R)^2 + \frac{z_0^2}{4 E^2 x_0^2}(\tan \theta_L - \tan \theta_R)^2$$

where in addition to the parameters identified above

E = the cloud chamber expansion ratio

$2x_0$ = the distance between the axes of the right and left camera lenses

z_0 = the distance to the camera lenses from the x, y, reference plane.

A graph was used to compute the $\sec \theta_T$ and is shown in figure 18, page 61 as the Secant θ Graph.

The number of plates from the upper fiducial reference to the point of the large interaction, including the fraction of the plate was tabulated.

The total path length of absorbing material passed through to a point of nuclear interaction, x , was computed by forming the product

$$x = \rho d n \sec \theta_T$$

$$= 23.1 \; n \sec \theta_T \text{ grams/(centimeter)}^2$$

where

ρ = the density of the steel

d = the thickness/plate

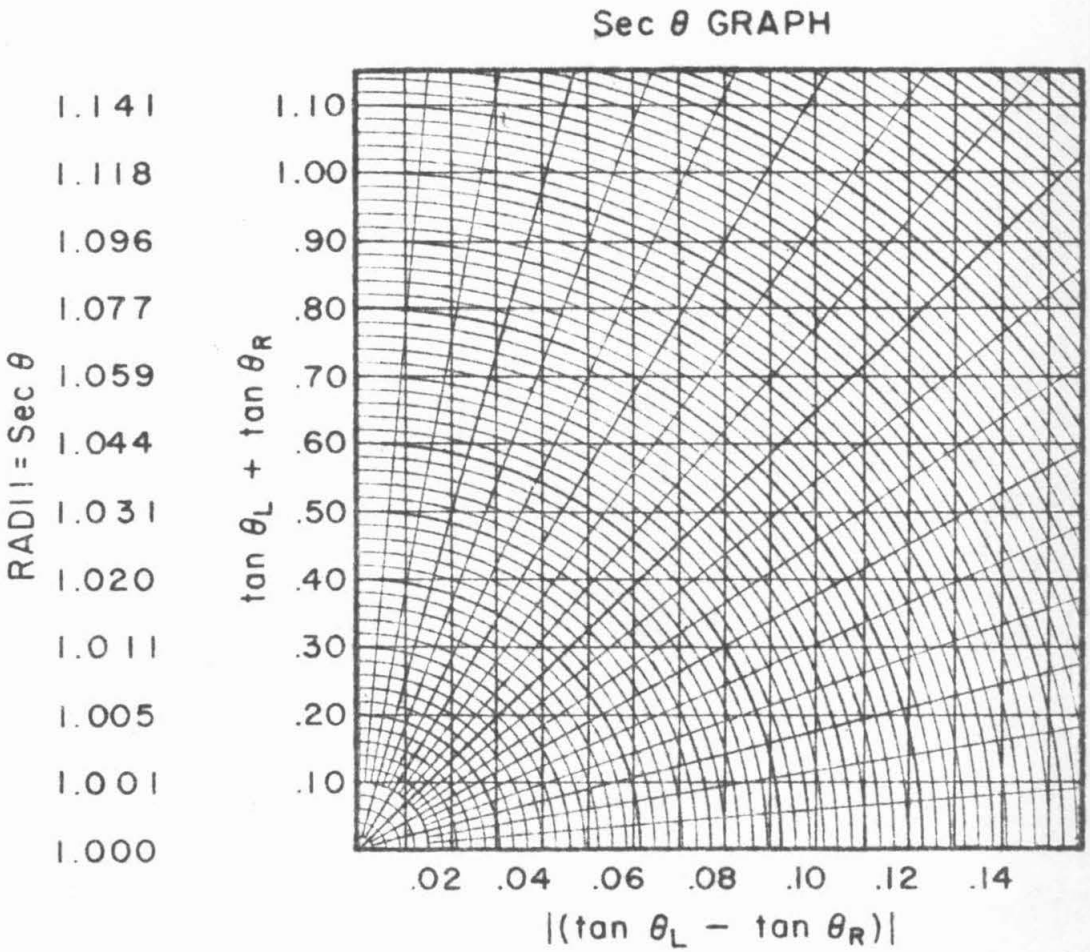

Figure 18. Secant θ Graph

n = the number of plates from the upper fiducial reference to the point of interaction

θ_T = the angle between the vertical in the chamber and the true path

and x has a new meaning from that established in the previous paragraphs as follows

x = the total path length from the fiducial reference to the point of nuclear interaction.

After computation of the path length, x, three cases had to be excluded, since the path length was in excess of the gate length, L_g. The gate length was established by selection criteria 2a and 3a above, as listed in Section VII. A. This left a total of six hundred thirty three (633) cases. The total path length, $\sum_{i=1}^{N} x_i$, for these cases, where

N = the number of cases

was formed and is tabulated below.

$$\sum_{i=1}^{N} x_i = 61{,}601.17 \text{ grams/(centimeter)}^2$$

measured from the fiducial reference to the point of the large interaction, including the fraction of a plate.

$$\sum_{i=1}^{N} x_i = 53{,}054.50 \text{ grams/(centimeter)}^2$$

measured from the fiducial reference to the point of the large interaction,

but excluding the fraction of the plate. That is the lower end of the track was taken to be the upper surface of the plate in which the nuclear interaction occurred.

For analytical purposes to be discussed, the path length through one plate was subtracted from each of the six hundred thirty-three (633) cases. For cases in plate two (2) such an operation was not possible, since the path length would have been negative. There were fifty-five (55) such cases. For the five hundred seventy-eight (578) remaining cases

$$\sum_{i=1}^{N} x_i = 39,311.12 \text{ grams/(centimeter)}^2$$

measured from the fiducial reference to the point of the large interaction minus one plate but excluding the fraction of the plate. That is, the lower end of the track was taken to be the upper surface of one plate above the plate in which the nuclear interaction occurred.

C. DATA FOR SMALL INTERACTIONS

A total of twenty-eight (28) cases of small interactions found above the large interaction, in accordance with the selection criteria of Section VII.A., were tabulated. Two (2) cases were questionable due to the wide angle of scatter of the penetrating particles created. They were possibly knock-on electron events instead of nuclear interactions. Thus twenty-six (26) cases of double nuclear interactions and two doubtful cases of double nuclear interactions were analysed. One of the large interactions had two distinct small interactions above it, both of which were in the same plate, as was determined by the points of intersection of the penetrating particles.

These interactions will be counted separately in succeeding analysis, making a grand total of twenty nine (29).

The angles of all particles from the small interaction were measured with respect to the line of flight of the incident primary particle creating the small interaction. An analysis was carried out to establish the ratio of the total energy to the rest mass energy in the center of mass system, γ_c.

From the angle transformation equation given in Appendix C

$$\tan \theta = \frac{\sin \theta^*}{\gamma_c(\cos \theta^* + \frac{\beta_c}{\beta^*})}$$

where

θ = the angle of a particle measured in the laboratory system

θ^* = the angle of a particle measure in the center of mass system

β^* = the velocity of a particle in the center of mass system divided by the velocity of light

β_c = the velocity of the center of mass itself (as seen in the laboratory system) divided by the velocity of light

$$\gamma_c = \frac{1}{\sqrt{1 - \beta_c^2}}$$

Using the above formula Castagnoli, Cortini, Franzinetti, Manfredini, and

Moreno[16] presented a convenient formulation for determining γ_c. Eliminating the ambiguity in sign by the use of absolute value signs and taking logarithms,

$$\ln \gamma_c = - \ln \left| \tan \theta \right| + \ln \frac{(1 - \cos^2 \theta^*)^{1/2}}{\left| \cos \theta^* + \frac{\beta_c}{\beta^*} \right|}$$

$$= - \ln \left| \tan \theta \right| + f \left(\cos \theta^*, \frac{\beta_c}{\beta^*} \right)$$

or taking the sum over n particles

$$\ln \gamma_c = - \frac{1}{n} \sum_{i=1}^{n} \ln \left| \tan \theta_i \right|$$

$$+ \frac{1}{n} \sum_{i=1}^{n} f \left(\cos \theta_i^*, \frac{\beta_c}{\beta_i^*} \right) .$$

By assuming that the angular distribution of all particles is symmetric with respect to the equatorial plane in the center of mass system, and by assuming that all n particles produced have no correlation between their angles nor between their energies of emission, Castagnoli, et.al. [16] as shown in Appendix F derived the following expression

$$\ln \gamma_c = - \frac{1}{n} \sum_{i=1}^{n} \ln \left| \tan \theta_i \right| \pm \frac{\sigma}{\sqrt{n}}$$

where in addition to the symbols used above

σ = the standard deviation.

This formulation has been used by Kaneko, Kusumoto, Matsumoto, and Takahata[17] as well as Teucher, Lohrmann, Haskin, and Schein[18]. The latter group in discussing nuclear interactions suggested the inclusion of an experimentally determined constant, C , in the formulation as follows

$$\ln \gamma_c = -\frac{1}{n} \sum_{i=1}^{n} \ln \left| \tan \theta_i \right| + \ln C$$

where

$$C = 0.7 \quad .$$

By applying the invariant equation for dynamics in the special theory of relativity given in Appendix B to a nucleon-nucleon collision for the center of mass and laboratory system,

$$(2M)^2 \gamma_c^2 = (M \gamma_1 + M)^2 - (M \beta_1 \gamma_1)^2$$

where in addition to the symbols identified above

M = the rest mass of the nucleon in energy units

β_1 = the velocity of the incident nucleus in the laboratory system divided by the velocity of light

$$\gamma_1 = \frac{1}{\sqrt{1 - \beta_c^2}} \quad .$$

Therefore by algebraic simplification,

$$E_1 = \gamma_1 M$$

$$= (2 \gamma_c^2 - 1) M$$

where in addition to the symbols identified above

E_1 = the total energy of the incident nucleon measured in the laboratory system.

The data for the small interactions is given in the following table. The first column lists the frame number. The second column lists the number of particles emanating from the small interaction. The third column lists $\ln \gamma_c$, as originally given by Castagnoli[16]. Column four tabulates E_1 as computed from column three. Column five lists γ_c, as

modified by Teucher[18] and co-workers of Schein. Column six tabulates E_1 as computed from column five.

Frame Number	Number of Particles	$\ln \gamma_c$ (C = 0)	E_1 (C=0)	$\ln \gamma_c$ (C =.7)	E_1 (C=.7)
93016	2	1.42	31.2	1.06	14.7
93034	3	2.09	121.5	1.73	58.7
93423	1;2V particles	———	———	———	———
94028	1	0.87	9.8	0.51	4.3
94204	3	2.59	332.4	2.23	161.3
94945	7	1.57	42.5	1.21	20.1
95022	9	1.24	21.5	0.88	10.0
95423	3	2.00	101.5	1.64	49.0
96483	4	1.75	61.1	1.39	29.2
96921	3	1.07	15.1	0.71	6.8
97512	7	1.60	45.0	1.24	21.5
97583	6	0.77	7.8	0.41	3.4
97610	4	1.23	21.0	0.87	9.8
97697	2	0.21	1.9	-0.15	0.5
98430	2	1.84	73.5	1.48	35.2
98635	2	3.70	3.07×10^3	3.34	1.49×10^3
98935	2	1.32	25.3	0.96	11.8
99674	1	4.05	6.18×10^3	3.69	3.01×10^3
99896	7	1.98	97.4	1.62	46.9
100199	1	1.64	49.0	1.28	23.4
100285	2	0.97	12.1	0.61	5.4
	2	1.88	79.6	1.52	38.2
100490	8	1.68	53.2	1.32	25.3
101653	4	2.10	124.3	1.74	60.0
101688	5	2.92	643.9	2.56	313.2
102396	2	2.89	606.2	2.53	294.5
102507	9	1.19	19.4	0.83	8.9
102685	3	2.32	193.5	1.96	93.6
103261	7	1.54	39.8	1.18	18.9

Extended data based on the use of a different constant, i. e., half the value by Teucher[18], was also computed. In the following table, the first column lists the frame number. The second column lists $\ln \gamma_c$ computed with the half value constant from that used by Teucher. Column three tabulates E_1 as computed from column two. Column four lists the estimate of E_1 by the author, and is based on the half angle of the cone subtended

by half of the charged particles and the use of the median angle formula. Column five lists the estimate of E_1 by Dr. Cowan.

Frame Number	ln γ_c (C = 0.35)	E_1 (C=0.35)	E_1(Est.) by Author	E_1(Est.) by Dr. Cowan
93016	0.37	3.0	10	<10
93034	1.04	14.1	20	20
93423	——	——	100	>100
94028	- 0.18	0.4	10	10
94204	1.54	39.9	10	10
94945	0.52	4.4	10	>100
95022	0.19	1.8	10	> 40
95423	0.95	11.6	20	>100
96483	0.70	8.6	10	< 10
96921	0.02	1.0	10	>100
97512	0.55	4.7	10	< 10
97583	- 0.28	0.1	5	< 10
97610	0.18	1.8	10	< 10
97697	- 0.84	——	5	10
98430	0.79	8.2	10	< 10
98635	2.65	374.9	>100	>100
98935	0.27	2.3	5	< 10
99674	3.00	755.9	>500	>500
99896	0.93	11.1	10	< 10
100199	0.59	5.2	10	10
100285	-0.08	0.7	5	10
	0.83	8.9	10	10
100490	0.63	5.7	10	30
101653	1.05	14.4	10	10
101688	1.87	78.0	100	>500
102396	1.84	73.5	80	>>10
102507	0.14	1.6	10	>500
102685	1.27	22.9	20	20
103261	0.49	4.1	10	> 20

It is to be noted that in all the preceding calculations involving applications or modifications of the Castagnoli formula that the secondary particle causing the large nuclear interaction has been excluded. Thus E_1 tabulated was the energy of the small interaction, and not the energy of the primary particle producing the interaction.

Additional data on the double nuclear interactions is given in the following table. Column one lists the frame number. Column two lists the sign of charge for the primary and secondary particles, respectively, causing the interactions. Column three lists the secant of the angle of the secondary particle with respect to the vertical. Column four lists the number of plates between the first and second interactions. Column five computes the path length based on the data of third and fourth columns.

Frame Number	Sign of Charge (Primary;Secondary)	Sec θ_T	Number of Plates to Secondary	Path Length of Secondary gm/cm^2
93016	Charged;Charged	1.029	1.9	45.16
93034	Charged;Charged	1.001	5.5	127.17
93423	Charged; Neutral	1.001	4.6	106.37
94028	Charged;Charged	1.008	1.3	30.26
94204	Charged;Charged	1.002	0.8	18.52
94945	Charged;Charged	1.013	1.9	35.18
95022	Neutral ;Charged	1.043	1.0	24.10
95423	Neutral ;Charged	1.007	5.5	127.94
96483	Neutral ;Charged	1.061	6.0	147.05
96921	Neutral ;Charged	1.048	0.6	14.52
97512	Charged; Neutral	1.010	0.7	16.33
97583	Charged;Charged	1.097	1.8	45.61
97610	Charged;Charged	1.033	0.6	14.32
97697	Charged;Charged	1.036	5.1	122.05
98430	Neutral ; Neutral	1.077	0.8	19.90
98635	Charged;Charged	1.042	3.6	86.65
98935	Charged;Charged	1.055	2.0	48.61
99674	Neutral ;Charged	1.001	1.3	30.06
99896	Charged;Charged	1.019	2.2	94.16
100199	Charged;Charged	1.014	1.0	163.96
100285	Charged; ?	1.004	—	—
	;Charged	1.004	2.4	55.66
100490	Charged; Neutral	1.000	3.2	23.10
101653	Charged;Charged	1.027	3.0	94.89
101688	Charged; Neutral	1.000	2.4	46.20
102396	Neutral ;Charged	1.055	1.8	97.48
102507	Charged;Charged	1.002	3.8	69.43
102685	Charged;Charged	1.095	6.8	25.29
103261	Neutral ; Neutral	1.001	3.0	69.36

D. CROSS-SECTION FOR SMALL INTERACTIONS IF UNRELATED TO LARGE INTERACTION

Additional selection criteria were established so as to include only those small interactions which were very much less energetic than the large interaction. The upper limit of energy permitted for a small interaction was 10 Bev, as set forth by two alternate criteria:

(a) Determination of the energy of the small interaction was made by use of the Castagnoli[16] formulation of Section VII.C. and the modification of that formula by the Schein co-workers[18].

(b) Independent estimates of the energy of the small interaction were made by two independent observers, Dr. Cowan and the author.

The small interaction shown in figure 17, page 56, occurred in plate eight (8). It contained two (2) particles. One was at 48° to the left of the line of flight of the primary particle and was minimum ionizing and non-penetrating. The other was at 3° to the right of the line of flight of the primary particle, was minimum ionizing and penetrated one plate. The primary particle causing the small interaction was charged. The secondary particle causing the large interaction was also charged and was at 0° to the line of flight of the primary particle. The Castagnoli[16] formulation yielded a calculated value for the energy of the small interaction of 31 Bev. As was pointed out by Schein this method tended to overestimate the energies under the spectrum independent approximation outlined in

Appendix F. Teucher[18] and co-workers of Schein employed an additive constant as a modification to the formulation as described in Section VII.C. Use of that modified formulation yielded an energy for the small interaction of 15 Bev. Castagnoli had pointed out on the basis of the Heisenberg and Fermi theories of meson production, that the additive factor was not necessarily constant. This fact had been recognized by Schein.

Since the number of particles in the interaction, and the corresponding energy of the interaction was much less that that being studied by the Schein group, an alternate additive constant, half that used by Schein, was employed in an endeavor to normalize the data of this experiment to estimates based on the median angle formula. Employing the new constant monotonically decreased all the calculated energies from that given by the Castagnoli formulation or the Schein modification of that formulation. The Castagnoli method in the energy range of this experiment, i.e., 10 Bev, had been used by Kaneko[17] et. al., but they failed to call out the adjustment of the Castagnoli formula used to obtain the forward-backward symmetry of the emitted angles. That the use of a constant, half that of the Schein value, i.e.,

$$C = 0.35$$

tended to underestimate some of the very low energy cases is evidenced by the negative value of $\ln \gamma_c$ for four (4) cases, one (1) of which was also negative with the Schein modification.

The small interaction of figure 17, page 56, had a calculated energy of 3 Bev employing the constant, half that of the Schein value. The esti-

mate of the author based on the median angle formula was 10 Bev. Dr. Cowan estimated the energy of this event at less than 10 Bev. This case typifies those double interactions which were included in the analysis of this section.

The question as to whether small interactions of the type illustrated were related to the large interactions below them and in their line of flight is a difficult one. If the incoming primary particle caused an iron nucleus to disintegrate with the subsequent emission of pi-mesons and nucleons, and if one of those pi-mesons or nucleons caused the second interaction, then one would say that the two events were related, the first causing the second. If on the other hand the primary particle struck an iron nucleon peripherally, it would cause a small number of pi-mesons or nucleons to be knocked out of the iron nucleus. Then the same primary nucleon could continue essentially in the same line of flight and the occurrence of a second interaction would be unrelated to the first, since there was no cause and effect relationship.

For either the related or the unrelated double interactions charge exchange phenomena were permissible processes. Frame number 96,483 was an example of a neutral primary and a charged secondary, which was interpreted as being a non-related double nuclear interaction.

The research investigation for non-related nuclear interactions was undertaken because of an anomalously large number on interactions in the cloud chamber data of the type illustrated in frame number 93,016 in figure 17, page 56, and 96,483. These cases illustrated an energy transfer to the secondary and its subsequent large nuclear interaction which was a

major portion of the total energy of the primary.

Even though the upper interaction appeared small in size, not all such interactions were lacking in energy. That there was some ambiguity as to the energy of the small interaction is shown by the discrepancies in the tabulated values of the calculated and estimated energies.

One such controversial case is shown in figure 19, page 74. The first interaction in plate two (2) was caused by a neutral primary particle, presumably a neutron, since the primary had to pass through plate one (1). The second interaction in plate seven (7) was caused by a charged secondary particle, presumably either a pi-meson or a proton. The first interaction contained only three particles. One of the particles was at 15^{o} to the left of the line of flight of the primary particle, was minimum ionizing and penetrated one (1) plate. The second particle was at 10^{o} to the left of the line of flight of the primary particle, was minimum ionizing and penetrated one (1) plate. The third particle was at 3^{o} to the left of the line of flight of the primary particle, was minimum ionizing and penetrated nine (9) plates.

The Castagnoli[16] formula yielded a calculated energy of 102 Bev. The Schein modification yielded a calculated energy of 49 Bev and the modification with the half value constant resulted in an energy of 11.6 Bev. The author estimated the energy as 20 Bev. Dr. Cowan, however, estimated the energy as in excess of 100 Bev. This case presented an extreme visual asymmetry about the line of flight of the secondary particle causing the lower large interaction. All the charged particles were to the left of that line of flight. Cases of this sort clearly needed interpretation on

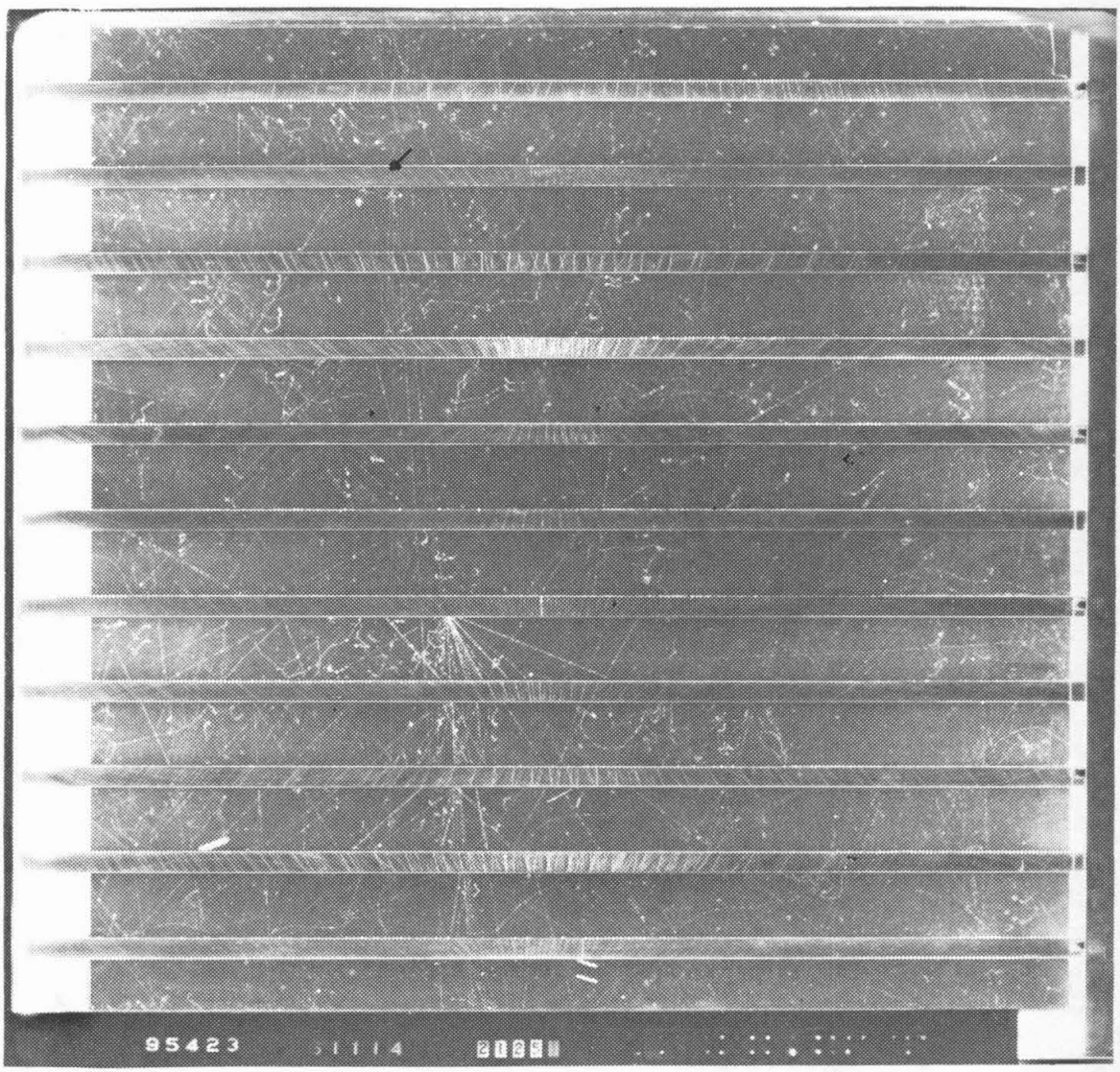

Figure 19. Double Nuclear Interaction
(Neutral - Charged)

the basis of close visual scrutiny as well as a mathematical analysis. Discrepancy in the visual estimates resulted from disagreement as to the importance given the particles emanating from the interaction.

The twenty-nine (29) cases of small nuclear interactions above large nuclear interactions were classified into three groups:

(1) Cases in which calculated and estimated energies were in general agreement that the small interaction was of 10 Bev or less,

(2) Cases in which the calculated and estimated energies were in general agreement that the small interaction had an energy greater than 10 Bev,

(3) Controversial cases in which either the calculated energy or one of the estimates was at great variance.

In the first category of general agreement that the energy of the small interaction was less than 10 Bev, there were fifteen (15) cases. These included frame 100285 which had two small interactions in one plate and was, therefore, counted twice in the summary. The only case of possible doubtful inclusion in this category was frame 94204 which had a moderately high calculated value on the basis of the modified Castagnoli formula. Both Dr. Cowan and the author agreed, however, that this case ought to be included since there was only one penetrating particle and since it penetrated but one plate.

The second category contained cases which were excluded for slightly different reasons: (a) Frames 93034 and 102685 were eliminated because the only penetrating particle in each frame was scattered at a

wide angle. The small interaction was probably electronic, and not nuclear. (b) Frame 93423, after a careful inspection, was re-evaluated as containing two (2) V particles, one with an origin barely below the plate, the other with an origin within the plate. Thus taken in conjunction with the remaining penetrating particle, the energy was most probably in excess of 10 Bev. (c) Frames 98635 and 99674 were observed to have narrow central cones for the small interaction and probably should have been excluded at the outset as being of high energy. (d) Frames 101688 and 102396 also possessed narrow cones and were excluded. The energy of the upper small interaction in these latter two cases, though in excess of 10 Bev, was probably less than the energy of the lower large interaction. As a total, therefore, seven (7) cases were definitely excluded from the analysis.

The last category was that of the controversial cases. Among these were the following: (a) Frame 95423 illustrated in figure 19, page 74, has already been discussed above. (b) Frames 95022, 100490, and 103261 all contained many particles but mostly at wide angles. Although some of the particles were at small angles in respect to the line of flight of the primary, there was no evidence in any of these cases for a narrow central cone. Visual interpretation and calculation yielded disagreement. The Castagnoli formulation would of course tend to decrease the energy estimate for an event containing particles with angles in excess of 45°, with respect to the line of flight of the primary. (c) Small interactions possibly interpretable as possessing a narrow cone are recorded in yet three additional cases. These controversial frames were 94945, 96921, and 102507. The

total of all controversial cases was seven (7).

Fifteen (15) cases of interactions less than 10 Bev, associated with a total of six hundred thirty-three (633) interactions in excess of 50 Bev, were found fulfilling the criteria as being independent and unrelated to other interactions. In the original analysis the total path length from the fiducial reference to the point of the large interaction, including the fraction of the plate traversed in which the large interaction occurred, was tabulated. Using the above value for total path length, the mean free path in iron, L_c, of a nucleon* with energy in excess of 50 Bev, between small interactions of less than 10 Bev, is given as $L_c = 61{,}601.17/15$ grams/(centimeter)^2. The mean free path, $L_c = (4.11 \pm 1.06) \times 10^3$ grams/(centimeter)^2, where the uncertainty has been established as the square root of the number of small interactions, divided by the number of small interactions.

Because of the difficulty in ascertaining whether or not there might be a small interaction in the same plate with and directly above the large interaction, a second tabulation of total path length was made eliminating the fraction of the plate. In fact, no small interactions were observed in the same plate with the large interaction. Elimination of the fraction of the plate to the large interaction also removed the uncertainty in estimating the fraction of the plate. The total path length thus was measured from the fiducial reference to the top of the plate above the second interaction. Using this new value of total path length, the mean free path in iron, L_c,

---

* The incident primary particles causing the interactions, though a mixture of pions and nucleons, will be referred to as nucleons for brevity and convenience in the succeeding discussion.

of a nucleon with energy in excess of 50 Bev, between small interactions of less than 10 Bev, which interactions were independent and unrelated to other nuclear interactions, is given as

$$L_c = \frac{53,054.50}{15}$$

$$= (3.54 \pm 0.91) \times 10^3 \text{ grams/(centimeter)}^2 \quad .$$

If the controversial cases were to be included the result would be given as

$$L_c = \frac{53,054.50}{22}$$

$$= (2.41 \pm 0.51) \times 10^3 \text{ grams/(centimeter)}^2 \quad .$$

In tabulating the non-related double interaction events it appeared that a large number were within one or two plates above the large interaction. Such should not be the case for random distribution along the total path length. Therefore, a test was performed as to the randomness. One plate of path length was subtracted from each of six hundred thirty-three (633) events thus establishing yet a third total path length as described in Section VII.B. This reduced the number of small interactions in the remaining path length. Using the reduced total path length and the reduced total of small interactions, the mean free path in iron, L_c, of a nucleon with energy in excess of 50 Bev, between small interactions of less than 10 Bev is given as

$$L_c = \frac{39,311.12}{9}$$

$$= (4.37 \pm 1.46) \times 10^3 \text{ grams/(centimeter)}^2 \quad .$$

This latter value was within the experimental error, and therefore the randomness of the location of the small interaction along the path length

was established.

The nucleon-nucleus cross-section, σ_c , for the process may be calculated by the formula given in Rossi[18] and presented previously in Section IV, namely,

$$\sigma_c = \frac{A}{N\ L_c}$$

where

A = the atomic weight of iron

N = the Avogadro number

L_c = the collision mean free path of small interaction as given above.

The total path length from the fiducial reference to the top of one plate above the large interaction was accepted as the best measurement. Using this path length a nucleon with energy in excess of 50 Bev possessed a nucleon-nucleus cross-section in iron for small interactions of less than 10 Bev, which interactions were independent and unrelated to other nuclear interactions, of

$$\sigma_c = 21.1 \pm 7.1 \text{ millibarns.}$$

To establish the nucleon-nucleon cross-section, σ , the transparency model of Brenner and Williams[20] was consulted. The nucleus was seen to be almost wholly transparent and the nucleon-nucleon cross-section was established as

$$\sigma = 0.38 \pm 0.13 \text{ millibarns.}$$

Correspondingly if the controversial cases were to be included and a calculation made for a path length reduced by one plate, the results

would be given as

$$L_c = \frac{39,311.12}{14}$$

$$= (2.81 \pm 0.75) \times 10^3 \text{ grams/(centimeters)}^2 ,$$

$$\sigma_c = 32.9 \pm 8.8 \text{ millibarns} ,$$

and

$$\sigma = 0.70 \pm 0.19 \text{ millibarns} .$$

When the seven (7) controversial cases were included in the foregoing computations, the nucleon-nucleon cross-section as obtained from the curve of Brenner and Williams was in a region of partial opacity. On the other hand, when only the firmly established cases were included, the portion of the curve used was that of nearly complete transparency. In fact, the nucleon-nucleon cross-section, σ, could be computed from the nucleon-nucleon cross-section, σ_c, by the relation for complete transparency, namely

$$\sigma_c = \sigma A .$$

The breakdown as to the nature of the primary and secondary particles giving rise to the small and large non-related nuclear interactions, respectively, is summarized below. The case of the small interaction in the same plate with the second interaction is of course excluded due to the inability to determine the sign of charge.

Primary Particle	Secondary Particle	Number of Firm Cases	Number of Cases, Firm and Controversial
Charged	Charged	11	13
Charged	Neutral	1	2
Neutral	Charged	1	4
Neutral	Neutral	1	2

The obvious excess in the number of the charged cases as compared to the neutral is probably attributable to the difference in scanning efficiency.

Recent theoretical work by Udgaonkar and Gell-Mann[19] has suggested that for high energy nuclear interactions there is an apparent increase in radius and of the transparency of the nucleon. On this basis of an essentially fuzzy nucleon as seen by an incoming energetic nucleon, one should expect an increase in the number of peripheral encounters.

The 50 Bev lower limit on the energy of the large nuclear interaction in the data analysis was chosen in order to be in an energy range above the capabilities presently available for machine accelerated nucleons. This lower limit probably also established that the incident nucleon was energetic enough to cause an increase in the radius of a nucleon in the iron as seen from the point of view of the incident nucleon.

With a 10 Bev upper limit on the energy of the small nuclear

interaction, only about seventeen percent of the total energy of the incident nucleon was transferred in the small interaction. This restriction established that the small nuclear interaction was probably the result of a peripheral encounter. The same incident nucleon would thus continue in essentially the same line of flight. A second nuclear interaction, large or small, on that line of flight then would be unrelated to the first nuclear interaction. In the research study performed, however, the second interaction was always greater than 50 Bev, since the energy of the second interaction was used to establish the energy of the incident nucleon, and thus in turn to identify the first interaction.

The interpretation of the small nuclear interactions as peripheral collisions and non-related to other nuclear interactions along the path length of the incident primary particle is strongly suggested.

VIII. SINGLE NUCLEAR INTERACTION ANALYSIS

The large nuclear interactions which had been tabulated in the double nuclear interaction analysis were also used for analytic purposes in a single nuclear interaction analysis.

A. SELECTION CRITERIA

Selection criteria for the cloud chamber events were established to determine:

(1) Collimation of the event to the vertical,

(2) The nuclear nature of the event,

(3) An energy for the event in excess of 50 Bev.

These prerequisites set forth the criteria outlined in Section VII.A. 1-3.

Certain of the double events presented ambiguity as to which point of nuclear interaction should be counted in establishing a total path length. This depended on whether one regarded those double interactions as related or unrelated. Therefore, it was necessary to establish:

(4) The elimination of ambiguous cases.

All those cases which were interpreted as being non-related on all bases could be included to the point of the second nuclear interaction. The two cases of wide scatter in the first interaction could likewise be included to the point of the second nuclear interaction. The remaining cases were ambiguous depending on the interpretation of the events. The following additional selection criteria were established:

(a) If on any basis of calculation or estimation both nuclear interactions, individually, could have

had an energy greater than 50 Bev, the case was excluded.

(b) If on any basis the event was interpreted as related, the event was excluded.

Clearly the two (2) criteria are not mutually exclusive. A list of those cases excluded under the two (2) criteria is listed below.

(a)	(b)
93423	———
94945	94945
———	95022
95423	95423
96921	96921
98635	———
99674	———
———	100490
101688	———
102396	———
102507	102507
———	103261

It was felt that no appreciable bias was introduced by elimination of the twelve (12) cases, since their elimination was in no way directly contingent upon the location in the cloud chamber.

B. DATA FOR INTERACTIONS

The six hundred thirty-three (633) cases which had been included in Section VII.B. were reduced by twelve (12) in accordance with the above selection criteria. This left a grand total of six hundred twenty-one (621) cases of unambiguous single interactions with energy in excess of 50 Bev. The total path length, $\sum_{i=1}^{N} x_i$, for these events,

where

x = the total path length for an event from the

fiducial reference to the point of nuclear interaction, including the fraction of a plate,

N = the number of events,

is given below

$$\sum_{i=1}^{N} x_i = 58{,}672.40 \text{ grams/(centimeter)}^2$$

Therefore

$$\frac{1}{N} \sum_{i=1}^{N} x_i = 94.48 \text{ grams/(centimeter)}^2$$

C. CROSS-SECTION FOR INTERACTIONS OF ENERGY GREATER THAN 50 BEV

The analysis of these data was carried out in accordance with the maximum likelihood procedure. This procedure as set forth by Fisher[21] was applied to the decay of radioactive substances by Peierls[22]. A clear statement of the procedure, including a method for computing standard deviation, is given by Bartlett[23]. This method has been used in cosmic ray applications by Alford[24], Strassenburg[25], and others.

The mean free path, L_c, in iron for nucleons in producing a nuclear interaction of greater than 50 Bev was calculated in accordance with the maximum likelihood procedure given in Appendix G. For this purpose the formulation for constant gate length, L_g, was used.

$$L_c = \frac{L_g}{e^{L_g/L_c} - 1} + \frac{1}{N} \sum_{i=1}^{N} x_i$$

where,

L_g = the gate length

N = the number of cases

x_i = the measured path length as tabulated on the preceding page.

The standard deviation, σ, was computed from the following formula,

$$\sigma = L_c \left[N \left\{ 1 - \frac{L_g^2}{L_c^2} \frac{e^{L_g/L_c}}{\left(e^{L_g/L_c} - 1\right)^2} \right\} \right]^{-1/2}$$

From the above formulae the mean free path, L_c, in iron for nucleons in producing a nuclear interaction of greater than 50 Bev was computed as

$$L_c = 390 \pm 108 \text{ grams/(centimeter)}^2 ,$$

where the error quoted is the standard deviation.

By use of the formula given in Rossi[18], the nucleon-nucleus cross-section, σ_c, was computed,

$$\sigma_c = \frac{A}{N L_c}$$

where

A = the atomic weight of iron

N = Avogadro's number

The value obtained was

$$\sigma_c = 0.24 \pm 0.07 \text{ barns.}$$

The value of the mean free path was high compared to the results of Brenner and Williams [20], as well as some previous work with data from the 5ft. x 5ft. x 2ft. cloud chamber. Recognition of this fact led to an investigation of possible bias or error in the selection of interactions with energy of 50 Bev or greater.

Consequently the data of the measured path length was tabulated by quarters of the absorbing material and by thirds in the temporal sequence. The distribution appeared to be the same for each of the three groups of two hundred eleven (211) cases. The maximum number of events occurred in the third quarter of absorbing material. It had been conjectured that the selection of a nine plate gate length might have led to the inclusion of events which were of energy less than 50 Bev, or even possibly the inclusion of some electron shower events, due to the inability to see the shower development near the bottom of the chamber. With the events maximizing in the third quarter, the number of such possible intruding errors would probably not account for the long mean free path.

If previous work with the 5ft. x 5ft. x 2ft. cloud chamber had not included some of the very high energy events, and if those events were of a smaller cross-section, the high mean free path of the current investigation might be explained.

The mean free path was only slightly smaller than the gate length in previous work with this chamber, and was longer than the

gate length in this analysis. This circumstance resulted in the computation of errors on the basis of the maximum likelihood procedure which were higher in the later analysis. Detailed inspection of the procedure reveals that the error assignment increases exponentially in the region used in this experiment. The assignment of symmetric errors, therefore, is probably misleading.

The maximum likelihood procedure likewise yields an exponentially increasing assignment to a value for the mean free path, with a linear increase in the measured value of the average path length to a point of nuclear interaction. A longer gate length, i.e., more absorbing material, would be desirable to obtain a more accurate value for the cross-section of nuclear interactions in excess of 50 Bev.

APPENDIX A

COUNTING RATE STUDY

A counting rate study was undertaken on rolls 13, 15, 16, and 17, except frames 7882 to 8225, where the hold time failed. During this period of operation various bias arrangements were used, namely, 15-45-45, 20-35-35, 15-35-35, and 15-30-30. The number of nuclear showers were tabulated for each of the various biases. Plots were made of

(1) Nuclear showers per running time, versus counts per running time;

(2) Nuclear showers per running time minus the three minute wait period per count, versus counts per running time minus the three minute wait period per count;

(3) Nuclear showers per count, versus the counts per running time.

The graphs are shown in the figure A on the next page. The results were self explanatory. A maximization of the nuclear events existed at the 15-35-35 bias setting and this was used for subsequent operation of the chamber with three geiger counter banks.

Upon removal of the top counter tray December 29, 1959 bias settings were adjusted to 0-60-60. An empirical investigation was again undertaken using bias settings as high as 0-80-80 and as low as 0-45-45. Most of the remaining data was obtained with a 0-50-50 bias.

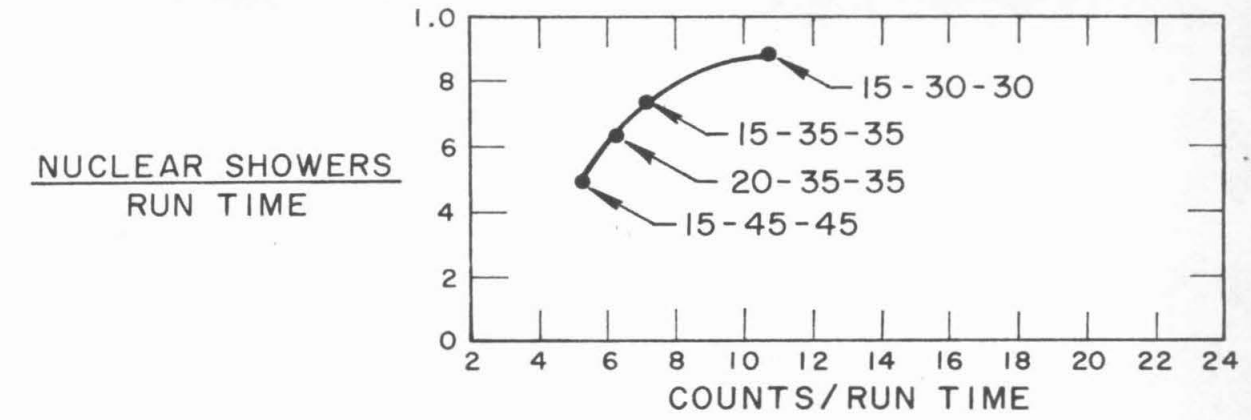

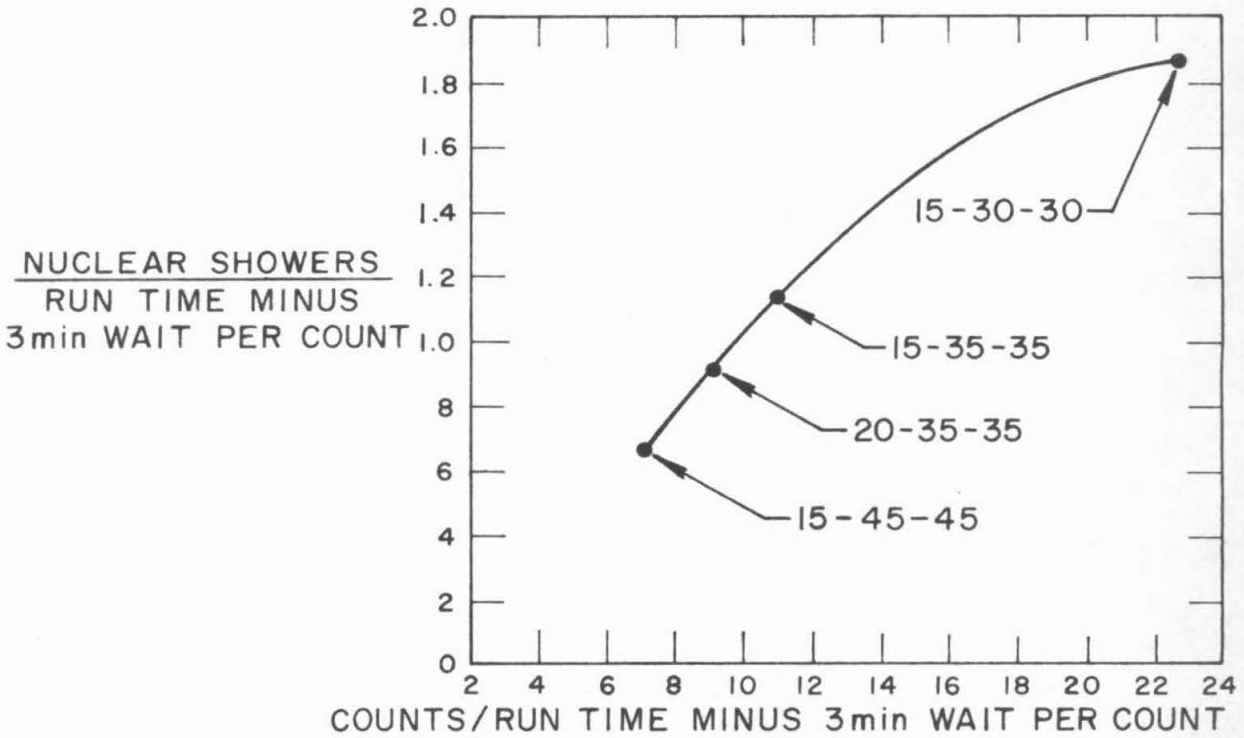

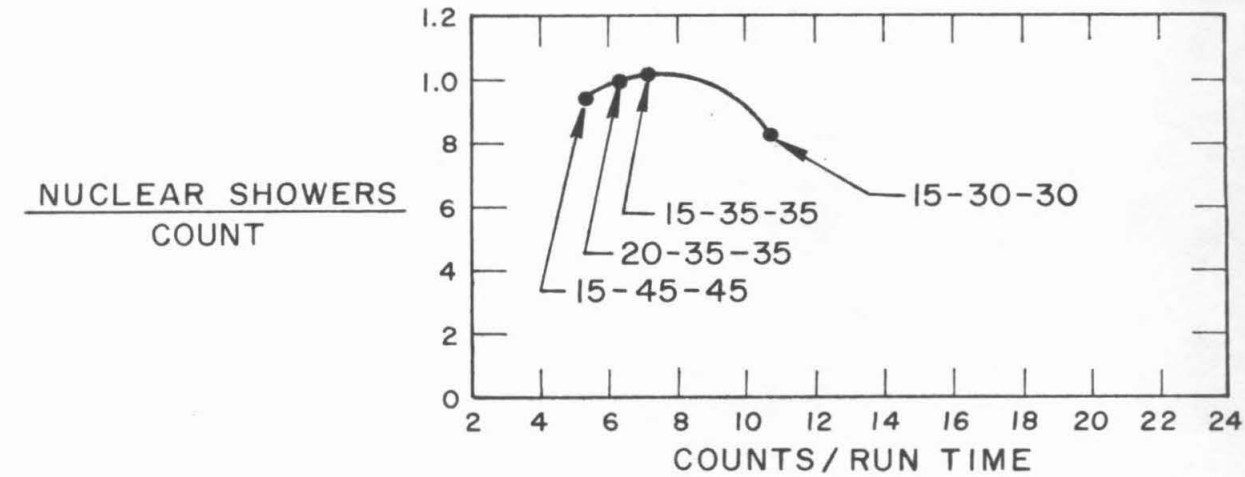

Figure A. Chamber Counting Rates

APPENDIX B

RELATIONS IN THE SPECIAL THEORY OF RELATIVITY

Basic relations of the Special Theory of Relativity are expressed below. Let the unprimed symbols be in an inertial laboratory coordinate system. Let primed symbols be in an inertial system of coordinates moving away from the laboratory system along the x axis with a relative velocity, v . Let the corresponding unprimed and primed coordinate axes be aligned.

Define the following quantities:

x, y, z = rectangular cartesian space coordinates

t = time coordinate

u_x, u_y, u_z = rectangular cartesian velocity coordinates corresponding to the space coordinates

M = rest mass of a particle (in energy units)

P_x, P_y, P_z = rectangular cartesian momentum of the particle corresponding to the space coordinates (in energy units)

E = total energy of the particle

T = kinetic energy of the particle

v = relative velocity of the two systems of coordinates

c = velocity of light

$\beta = v/c$

$\gamma = (1 - \beta^2)^{-1/2}$.

$$\tau = ct$$

$$\beta_x = \frac{u_x}{c}$$

$$\gamma_x = (1 - \beta_x)^{-1/2}$$

With a similar set of definitions for the primed system, space-time relations for two systems of rectangular cartesian coordinates in uniform translational motion along their respective x axes are given by

$$x' = \gamma(x - \beta\tau) \qquad x = \gamma(x' + \beta\tau')$$

$$y' = y$$

$$z' = z$$

$$\tau' = \gamma(\tau - \beta x) \qquad \tau = \gamma(\tau' + \beta x') \quad \text{Eqns. 1}$$

The velocity relations are simply deduced by differentation and substitution as

$$u'_x = \frac{dx'}{dt'} = \frac{u_x - v}{1 - \frac{u_x v}{c^2}} \qquad u_x = \frac{dx}{dt} = \frac{u'_x + v}{1 + \frac{u_x v}{c^2}}$$

$$u'_y = \frac{dy'}{dt'} = \frac{u_y}{\gamma\left(1 - \frac{u_x v}{c^2}\right)} \qquad u_y = \frac{dy}{dt} = \frac{u'_y}{\gamma\left(1 + \frac{u'_x v}{c^2}\right)}$$

$$u'_z = \frac{dz'}{dt'} = \frac{u_z}{\gamma\left(1 - \frac{u_x v}{c^2}\right)} \qquad u_z = \frac{dz}{dt} = \frac{u'_z}{\gamma\left(1 + \frac{u'_x v}{c^2}\right)} \quad \text{Eqns. 2}$$

Momentum - energy relations are similarly given by

$$P'_x = \gamma(P_x - \beta E) \qquad P_x = \gamma (P'_x + \beta E')$$

$$P'_y = P_y$$

$$P'_z = P_z$$

$$E' = \gamma (E - \beta P_x) \qquad E = \gamma (E' + \beta P'_x).$$

Eqns. 3

As may be seen by combining the above equations .

$$E^2 - (P_x^2 + P_y^2 + P_z^2) = \text{Const.}$$

or in general by summing over many particles

$$(\sum_i E_i)^2 - (\sum_i P_i)^2 = \text{Const.}$$

for all systems of inertial coordinates this difference is invariant.

The general conservation principles operative in special relativity within any particular conservative inertial system are

$$\sum_i P_i = \text{Const.} \qquad \text{Eq. 4}$$

$$\sum_i E_i = \sum_i (T_i + M_i) = \text{Const.} \qquad \text{Eq. 5}$$

where the rest masses are also invariant for all systems of coordinates.

By consideration of a special system in which one coordinate system is attached to a particle moving with a velocity $u_x = v$ one can derive several relations of general interest. In such a system

$$T' = 0.$$

Therefore by Eq. 5

$$E' = M$$

and one obtains the general relation for any inertial coordinate system

$$E^2 - P^2 = M^2 \quad . \qquad \text{Eq. 6}$$

By use of the momentum-energy relations of Eqns. 3 and since in the special coordinate system under consideration

$$P' = 0$$

and

$$E' = M$$

one has

$$P_x = \gamma\beta M \qquad \text{Eq. 7}$$

$$E = \gamma M \quad . \qquad \text{Eq. 8}$$

It should be recalled that $u_x = v$ in the special frame of reference which was chosen. That is the velocity of the second frame with respect to the first is also the velocity of the particle in the first frame of reference. Therefore

$$P_x = \gamma_x \beta_x M \qquad \text{Eq. 9}$$

$$E = \gamma_x M \qquad \text{Eq. 10}$$

These latter relations are perfectly general within any particular coordinate system.

APPENDIX C

ANGLE TRANSFORMATION FOR PARTICLES

The angles appropriate to the paths taken by particles traveling with relativistic speeds as seen from different coordinate systems are expressed below.

Use the identification of symbols as in Appendix B. Assume one coordinate system to be the center of mass system and designate quantities within that system by starred superscripts. Assume the other coordinate system to be the laboratory system and allow quantities within that system to be unstarred. The relative velocity of the two systems is thus the velocity of the center of mass. Designate quantities appropriate to the center of mass coordinate system itself by a subscript c. Thus typically of all symbols

$\beta = \frac{u}{c}$ = velocity of a particle in the laboratory system divided by the velocity of light

$\beta^* = \frac{u^*}{c}$ = velocity of a particle in the center of mass system divided by the velocity of light

$\beta_c = \frac{v}{c}$ = velocity of the center of mass itself (as seen in the laboratory system) divided by the velocity of light

$\beta_1 = \frac{u_1}{c}$ = velocity of the incident particle in the laboratory system divided by the velocity of light.

Also define

M_1 = rest mass of the incident particle (in energy units)

M_2 = rest mass of the target particle (in energy units)

If the angles θ and θ^* are measured from their respective x and x^* axes one has

$$u_x = u \cos \theta \qquad \text{Eq. 1}$$

$$u_y = u \sin \theta \qquad \text{Eq. 2}$$

$$u_x^* = u^* \cos \theta^* \qquad \text{Eq. 3}$$

$$u_y^* = u^* \sin \theta^* . \qquad \text{Eq. 4}$$

The motion of the center of mass coordinate system is assumed to take place along the x and x^* axes. Thus by the velocity transformation formulae are

$$u_x = \frac{u_x^* + v}{1 + \frac{u_x^* v}{c^2}} \qquad \text{Eq. 5}$$

$$u_y = \frac{u_y^*}{\gamma_c \left(1 + \frac{u_x^* v}{c^2}\right)} . \qquad \text{Eq. 6}$$

The definition of tangent θ from Equations 1 and 2 is given by

$$\tan \theta = \frac{u_y}{u_x} . \qquad \text{Eq. 7}$$

Upon substitution of Equations 3, 4, 5, and 6 in Equation 7 so as to eliminate u_x , u_y , u_x^* and u_y^*

$$\tan \theta = \frac{u^* \sin \theta^*}{\gamma_c \, (u^* \cos \theta^* + v)}$$

or

$$\tan \theta = \frac{\sin \theta^*}{\gamma_c \left(\cos \theta^* + \frac{\beta_c}{\beta^*} \right)} \quad \text{Eq. 8}$$

Using the invariant expression

$$\left(\sum_i E_i \right)^2 - \left(\sum_i P_i \right)^2 = \text{Const.}$$

as applied to the center of mass seen from the laboratory system, and to the individual particles seen in the laboratory system

$$(M_1 + M_2)^2 \gamma_c^2 - 0 = (M_1 \gamma_1 + M_2)^2 - (M_1 \beta_1)^2 \gamma_1^2 .$$

Upon expansion and simplification

$$\gamma_c = \frac{(M_1^2 + M_2^2 + 2 M_1 M_2 \gamma_1)^{1/2}}{M_1 + M_2} . \quad \text{Eq. 9}$$

The velocity of the center of mass is

$$\beta_c = \left(\frac{2 M_1 M_2 (\gamma_1 - 1)}{M_1^2 + M_2^2 + 2 M_1 M_2 \gamma_1} \right)^{1/2} . \quad \text{Eq. 10}$$

The general expression for the angle transformation is given by

$$\tan \theta = \frac{(M_1 + M_2) \sin \theta^*}{(M_1^2 + M_2^2 + 2 M_1 M_2 \gamma_1)^{1/2} \cos \theta^* + \frac{[2 M_1 M_2 (\gamma_1 - 1)]^{1/2}}{\beta^*}} . \quad \text{Eq. 11}$$

In the special case where $M_1 = M_2$ this becomes

$$\tan \theta = \frac{\sin \theta^*}{\left(\frac{\gamma_1 + 1}{2} \right)^{1/2} \cos \theta^* + \left(\frac{\gamma_1 - 1}{2} \right)^{1/2} \frac{1}{\beta^*}} \quad \text{Eq. 12}$$

or

$$\tan \theta = \frac{\sin \theta^*}{\left(\frac{\gamma_1 + 1}{2}\right)^{1/2}\left[\cos \theta^* + \left(\frac{\gamma_1 - 1}{\gamma_1 + 1}\right)^{1/2} \frac{1}{\beta^*}\right]} \quad . \qquad \text{Eq. 13}$$

Further if the velocity of the incoming particle is large, the total energy, compared to the rest mass energy, is large

$$\frac{\gamma_1 + 1}{2} \cong \frac{W_1}{2 M_1} \qquad \text{Eq. 14}$$

and

$$\left(\frac{\gamma_1 - 1}{\gamma_1 + 1}\right)^{1/2} \frac{1}{\beta^*} \cong 1 \quad . \qquad \text{Eq. 15}$$

Therefore for a very energetic incoming particle hitting a target of equal mass

$$\tan \theta = \left(\frac{2 M_1}{W_1}\right)^{1/2} \frac{\sin \theta^*}{\cos \theta^* + 1}$$

$$\tan \theta = \left(\frac{2 M_1}{W_1}\right)^{1/2} \tan \frac{\theta^*}{2} \quad . \qquad \text{Eq. 16}$$

APPENDIX D

DYNAMICS OF NEUTRAL PI MESIC DECAY

The relativistic dynamics of the decay of a neutral pi meson into two gamma rays

$$\pi^{o} = \gamma_1 + \gamma_2$$

may be set forth on the basis of the conservation of total energy and the conservation of momentum.

Define the following quantities in the laboratory system of coordinates

M_π = rest mass of the π^{o} meson (in energy units)

P_π = momentum of the π^{o} meson (in energy units)

E_π = total energy of the π^{o} meson

O = rest mass of γ_1 and γ_2

P_1, P_2 = momenta of γ_1 and γ_2, respectively, (in energy units)

E_1, E_2 = total energy of γ_1 and γ_2, respectively

θ = angle between the line of flight of γ_1 and γ_2.

Before decay After decay

Figure B. Pi Mesic Decay

By conservation of total energy

$$E_\pi = E_1 + E_2$$

but by definition of total energy in Equation 6, Appendix B

$$E_\pi = \sqrt{M_\pi^2 + P_\pi^2}$$

$$E_1 = \sqrt{0 + P_1^2} = P_1$$

$$E_2 = \sqrt{0 + P_2^2} = P_2$$

and therefore the energy conservation becomes upon substitution of the foregoing definitions

$$\sqrt{M_\pi^2 + P_\pi^2} = P_1 + P_2$$

or more conveniently in terms of the total energies of γ_1, γ_2

$$\sqrt{M_\pi^2 + P_\pi^2} = E_1 + E_2 . \qquad \text{Eq. 1}$$

By conservation of momentum before and after the decay and by use of the law of cosines

$$P_\pi^2 = P_1^2 + P_2^2 + 2 P_1 P_2 \cos\theta$$

or in terms of the total energies of γ_1 and γ_2

$$P_\pi^2 = E_1^2 + E_2^2 + 2 E_1 E_2 \cos\theta . \qquad \text{Eq. 2}$$

Combining Equations 1 and 2 so as to eliminate P_π

$$M_\pi^2 = 2 E_1 E_2 (1 - \cos\theta)$$

or

$$\sin\frac{\theta}{2} \qquad \frac{M_\pi}{2\sqrt{E_1 E_2}} . \qquad \text{Eq. 3}$$

In the special case when the energies of the two gamma rays are equal

$$E_{\pi} = 2 E_1 = 2 E_2$$

and therefore

$$\sin \frac{\theta}{2} = \frac{M_{\pi}}{E_{\pi}} . \qquad \text{Eq. 4}$$

APPENDIX E

CHAMBER GEOMETRY CALCULATIONS

In order to calculate the actual path length traversed by a particle incident to the cloud chamber used in the experiment, it is necessary to obtain a relationship between the angles seen in the conical projection by the camera lenses and the orthogonal projection with respect to the chamber walls.

Define the following quantities taking the orthogonal axes at the center of the chamber as seen in figure C on the following page

x_{1T}, y_{1T}, z_{1T} = the orthogonal coordinates of the point, P_1

x_{1L}, y_{1L} = the conical projection coordinates on x, y reference plane of the point, P_1, as seen from the left camera lens

x_{1R}, y_{1R} = the conical projection coordinates on x, y reference plane of the point, P_1, as seen from the right camera lens.

A similar set of coordinates, i.e., x_{2T}, y_{2T}, z_{2T}, etc. may be defined for the point, P_2.

$2x_0$ = the distance between the axes of the right and left camera lenses

z_0 = the distance to the camera lenses from the x, y reference plane

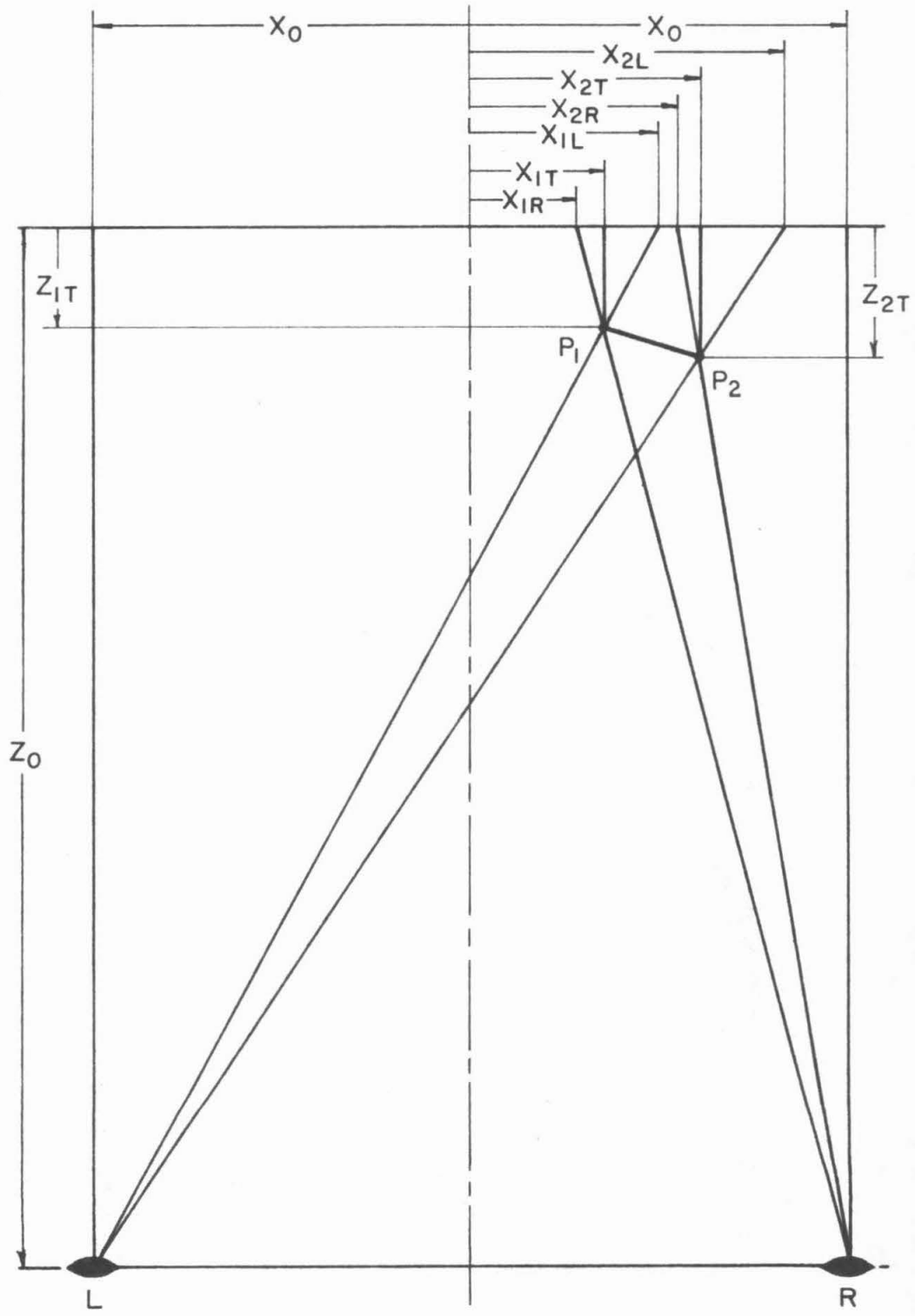

Figure C. Chamber Geometry

$$x_1 = \frac{x_{1L} + x_{1R}}{2} \qquad \text{Eq. 1 a}$$

$$\Delta_1 = \frac{z_{1T}}{z_0} \qquad \text{Eq. 1 b}$$

$$x_2 = \frac{x_{2L} + x_{2R}}{2} \qquad \text{Eq. 2 a}$$

$$\Delta_2 = \frac{z_{2T}}{z_0} \; . \qquad \text{Eq. 2 b}$$

Since the two lenses are at the same height,

$$y_1 = y_{1L} = y_{1R}$$

$$y_2 = y_{2L} = y_{2R} \; .$$

From the geometry by similar triangles the relevant expressions are

$$\frac{x_{1L} - x_{1T}}{x_0 + x_{1L}} = \frac{z_{1T}}{z_0} \qquad \text{Eq. 3}$$

$$\frac{x_{1T} - x_{1R}}{x_0 - x_{1R}} = \frac{z_{1T}}{z_0} \qquad \text{Eq. 4}$$

$$\frac{x_{2L} - x_{2T}}{x_0 + x_{2L}} = \frac{z_{2T}}{z_0} \qquad \text{Eq. 5}$$

$$\frac{x_{2T} - x_{2R}}{x_0 - x_{2R}} = \frac{z_{2T}}{z_0} \; . \qquad \text{Eq. 6}$$

Eliminating x_0 from Equations 3 and 4 and by use of the definition of Equation 1

$$x_{1T} = x_1 (1 - \Delta_1) \; . \qquad \text{Eq. 7}$$

Similarly eliminating x_0 from Equations 5 and 6 and by use of definition of Equation 2

$$x_{2T} = x_2 \ (1 - \Delta_2) . \qquad \text{Eq. 8}$$

Similar relations may be developed for the y coordinates

$$y_{1T} = y_1 \ (1 - \Delta_1). \qquad \text{Eq. 9}$$

$$y_{2T} = y_2 \ (1 - \Delta_2). \qquad \text{Eq. 10}$$

The angles measured on the film with respect to a vertical are

$$\tan \theta_L = \frac{x_{2L} - x_{1L}}{y_2 - y_1} \qquad \text{Eq. 11}$$

$$\tan \theta_R = \frac{x_{2R} - x_{1R}}{y_2 - y_1} . \qquad \text{Eq. 12}$$

The trigonometric function by which the vertical path length need be multiplied to get the actual path length traversed is the sec θ_T where

θ_T = the angle between the vertical in the chamber and the actual path.

$$\sec^2 \theta_T = 1 + \frac{(x_{2T} - x_{1T})^2 + (z_{2T} - z_{1T})^2}{(y_{2T} - y_{1T})^2} .$$

By substitution of Equations 7, 8, 9, and 10

$$\sec^2 \theta_T \quad 1 \quad \frac{[x_2 (1 - \Delta_2) - x_1 (1 - \Delta_1)]^2 + z_0^2 (\Delta_2 - \Delta_1)^2}{[y_2 (1 - \Delta_2) - y_1 (1 - \Delta_1)]^2} . \qquad \text{Eq. 13}$$

Special case. For the case of no z depth difference

$$\Delta_1 = \Delta_2$$

and

$$\sec^2\theta_T = 1 + \frac{(x_2 - x_1)^2}{(y_2 - y_1)^2} .$$

Upon substituting the relations given in Equations 1 a, 2 a, 11 and 12

$$\sec^2\theta_T = 1 + \left[\frac{1}{2}(\tan\theta_L + \tan\theta_R)\right]^2 . \qquad \text{Eq. 14}$$

General case. Equation 13 may be expanded and written

$$\sec^2\theta_T = 1 \frac{(x_2 - x_1)^2 - 2(x_2 - x_1)(x_2\Delta_2 - x_1\Delta_1) + (x_2\Delta_2 - x_1\Delta_1)^2 + z_0^2(\Delta_2 - \Delta_1)^2}{(y_2 - y_1)^2\left(1 - \frac{y_2\Delta_2 - y_1\Delta_1}{y_2 - y_1}\right)^2} .$$

Eq. 15

If the expression

$$\frac{(\Delta_2 - \Delta_1)y_1}{y_2 - y_1} < 1 - \Delta_2$$

which is the case for small z depth differences, the denominator of $\sec^2\theta_T$ may be expanded to the second order in Δ as follows

$$\frac{1}{\left(1 - \frac{y_2\Delta_2 - y_1\Delta_1}{y_2 - y_1}\right)^2} = 1 + \frac{2(y_2\Delta_2 - y_1\Delta_1)}{y_2 - y_1}$$

$$+ \frac{3(y_2\Delta_2 - y_1\Delta_1)^2}{(y_2 - y_1)^2} + 0(\Delta^3) .$$

Eq. 16

Retaining terms only to the second order upon substituting Equation 16 in Equation 15

$$\sec^2 \theta_T = 1 + \frac{(x_2 - x_1)^2}{(y_2 - y_1)^2} - 2\frac{(x_2 - x_1)}{(y_2 - y_1)} \frac{(x_2 \Delta_2 - x_1 \Delta_1)}{(y_2 - y_1)}$$

$$+ \frac{(x_2 \Delta_2 - x_1 \Delta_1)^2}{(y_2 - y_1)^2} + s_0^2 \frac{(\Delta_2 - \Delta_1)^2}{(y_2 - y_1)^2}$$

$$+ 2\frac{(x_2 - x_1)^2}{(y_2 - y_1)^2} \frac{(y_2 \Delta_2 - y_1 \Delta_1)}{(y_2 - y_1)}$$

$$- \frac{2(x_2 - x_1)}{(y_2 - y_1)} \frac{(x_2 \Delta_2 - x_1 \Delta_1)}{(y_2 - y_1)} \frac{(y_2 \Delta_2 - y_1 \Delta_1)}{(y_2 - y_1)}$$

$$\frac{3(x_2 - x_1)^2}{(y_2 - y_1)^2} \frac{(y_2 \Delta_2 - y_1 \Delta_1)^2}{(y_2 - y_1)^2} \quad \text{Eq. 17}$$

Eliminating x_{1T} from Equations 3 and 4 and by use of the definition of Equation 1 b

$$\Delta_1 = \frac{x_{1L} - x_{1R}}{2x_0 + x_{1L} - x_{1R}}$$

$$\cong \frac{x_{1L} - x_{1R}}{2x_0} \quad \text{Eq. 18}$$

Eliminating x_{2T} from Equation 5 and 6 and by use of the definition of Equation 2 b

$$\Delta_2 = \frac{x_{2L} - x_{2R}}{2x_0 + x_{2L} - x_{2R}}$$

$$\cong \frac{x_{2L} - x_{2R}}{2x_0} \quad \text{Eq. 19}$$

Therefore from Equations 18 and 19

$$\frac{\Delta_2 - \Delta_1}{y_2 - y_1} = \frac{1}{2 x_0} \left(\frac{x_{2L} - x_{1L}}{y_2 - y_1} - \frac{x_{2R} - x_{1R}}{y_2 - y_1} \right)$$

by substitution of the definitions of Equations 11 and 12

$$\frac{\Delta_2 - \Delta_1}{y_2 - y_1} = \frac{1}{2 x_0} \left(\tan \theta_L - \tan \theta_R \right). \qquad \text{Eq. 20}$$

Correction terms may be approximated as

$$\frac{x_2 \Delta_2 - x_1 \Delta_1}{y_2 - y_1} \cong \frac{x}{2 x_0} \left(\tan \theta_L - \tan \theta_R \right) \qquad \text{Eq. 21}$$

$$\frac{y_2 \Delta_2 - y_1 \Delta_1}{y_2 - y_1} \cong \frac{y}{2 x_0} \left(\tan \theta_L - \tan \theta_R \right) \qquad \text{Eq. 22}$$

where

$$x = \frac{x_2 + x_1}{2}$$

and

$$y = \frac{y_2 + y_1}{2} .$$

By substituting Equations 20, 21 and 22 in Equation 17

$$\sec^2\theta_T = 1 + \frac{1}{4}(\tan\theta_L + \tan\theta_R)^2$$

$$- \frac{x}{2x_0}(\tan\theta_L + \tan\theta_R)(\tan\theta_L - \tan\theta_R)$$

$$+ \frac{x^2}{4x_0^2}(\tan\theta_L - \tan\theta_R)^2$$

$$+ \frac{z_0^2}{4x_0^2}(\tan\theta_L - \tan\theta_R)^2$$

$$+ \frac{y}{4x_0}(\tan\theta_L + \tan\theta_R)^2(\tan\theta_L - \tan\theta_R)$$

$$- \frac{xy}{4x_0^2}(\tan\theta_L + \tan\theta_R)(\tan\theta_L - \tan\theta_R)^2$$

$$+ \frac{3y^2}{16x_0^2}(\tan\theta_L + \tan\theta_R)^2(\tan\theta_L - \tan\theta_R)^2 .$$

If corrections of Equations 21 and 22 are neglected, one has the useful approximation

$$\sec^2\theta_T = 1 + \frac{1}{4}(\tan\theta_L + \tan\theta_R)^2$$

$$+ \frac{z_0^2}{4x_0^2}(\tan\theta_L - \tan\theta_R)^2 .$$

In order to correct for the expansion ratio, E , the formula must be modified to

$$\sec^2\theta_T = 1 + \frac{1}{4}(\tan\theta_L + \tan\theta_R)^2$$

$$+ \frac{z_0^2}{4E^2x_0^2}(\tan\theta_L - \tan\theta_R)^2 .$$

APPENDIX F

PRIMARY PARTICLE ENERGY CALCULATION

The energy of the primary particle causing a nuclear interaction may be calculated by a method developed by Castagnoli, et. al[16]. The method is based on the following assumptions: (1) the angular distribution of the particles emitted from the interaction is symmetric with respect to the equatorial plane, and (2) there is no correlation between the angles, nor between the energies of emission, for the particles.

Starting with the angle transformation equation as given in Appendix C

$$\gamma_c = \frac{1}{\tan \theta} \frac{(1 - \cos^2 \theta^*)^{1/2}}{\left(\cos \theta^* + \frac{\beta_c}{\beta^*}\right)} \qquad \text{Eq. 1}$$

where the symbols have been identified in Appendix C, and the angles θ and θ^* are measured with respect to the line of flight of the primary particle.

By employing the absolute value signs so as to eliminate the algebraic sign ambiguity and by taking logarithms, the following result was obtained

$$\ln \gamma_c = - \ln \left| \tan \theta \right| + \ln \frac{(1 - \cos^2 \theta^*)^{1/2}}{\left| \cos \theta^* + \frac{\beta_c}{\beta^*} \right|} \qquad \text{Eq. 2}$$

Taking the sum over n particles yielded

$$\ln \gamma_c = - \frac{1}{n} \sum_{i=1}^{n} \ln \left| \tan \theta_i \right|$$

$$+ \frac{1}{n} \sum_{i=1}^{n} \frac{(1 - \cos^2 \theta_i^*)^{1/2}}{\left| \cos \theta_i^* + \frac{\beta_c}{\beta_i^*} \right|} \quad . \qquad \text{Eq. 3}$$

By making the substitutions

$$\cos \theta_i^* = \mu_i$$

$$\sin \theta_i^* = (1 - \mu_i^2)^{1/2} \qquad \text{Eqns. 4}$$

the equation became

$$\ln \gamma_c = - \frac{1}{n} \sum_{i=1}^{n} \ln \left| \tan \theta_i \right|$$

$$+ \frac{1}{n} \sum_{i=1}^{n} \ln \frac{(1 - \mu_i^2)^{1/2}}{\left| \mu_i + 1 \right|} \qquad \text{Eq. 5}$$

where it is assumed that

$$\frac{\beta_c}{\beta^*} = 1 \quad . \qquad \text{Eq. 6}$$

By making the further identification

$$\mu_i = \tanh \phi_i$$

$$(1 - \mu_i^2)^{1/2} = \frac{1}{\cosh \phi_i} \qquad \text{Eqns. 7}$$

The equation simplified to

$$\ln \gamma_c = - \frac{1}{n} \sum_{i=1}^{n} \ln \left| \tan \theta_i \right|$$

$$- \frac{1}{n} \sum_{i=1}^{n} \phi_i \quad . \qquad \text{Eq. 8}$$

By going to a continuous variable, one could ask the probability $F(\phi)\, d\phi$ that the value of ϕ fell in a given interval $d\phi$, or one could ask the equivalent question of the probability $f(\mu)\, d\mu$ of finding a particle track in $d\mu$. Mathematically,

$$F(\phi)\, d\phi = f(\mu) \frac{d\mu}{d\phi}\, d\phi \qquad \text{Eq. 9}$$

$$= f(\tanh \phi) \frac{d\phi}{\cosh^2 \phi} \quad .$$

Since the first assumption above conditioned the distribution of the particles as symmetric with respect to the equatorial plane, $F(\phi)$ was assumed to be an even function of ϕ, and therefore,

$$\overline{\phi} = \int_{-\infty}^{\infty} \phi \quad F(\phi)\, d\phi \qquad \text{Eq. 10}$$

$$= 0 \quad .$$

that is

$$\frac{1}{n} \sum_{i=1}^{n} \phi_i = 0 \quad . \qquad \text{Eq. 11}$$

The fluctuation around the average value of zero may be calculated by the conventional method of the second moment. The variance, σ^2, is given by

$$\sigma^2 = \int_{-\infty}^{\infty} \phi^2 \, F(\phi)\, d\phi \quad . \qquad \text{Eq. 12}$$

The general relation for γ_c is therefore given by

$$\ln \gamma_c = - \frac{1}{n} \sum_{i=1}^{n} \ln \left| \tan \theta_i \right| \pm \frac{\sigma}{\sqrt{n}} \quad . \qquad \text{Eq. 13}$$

Hence the primary particle energy is calculable.

APPENDIX G

MAXIMUM LIKELIHOOD CALCULATIONS

The method of maximum likelihood can be used for a distribution of ranges to the point of a nuclear interaction when the gate length for observing such interactions is finite. This method is particularly necessary when the gate length is only slightly larger than the average range of a particle to a point of nuclear interaction.

Let the following definitions be set forth,

$$P(x) = \frac{N_t(x)}{N_o(0)}$$

$N_t(x)$ = the total number of primary particles at a distance, x , in the chamber from the upper fiducial reference of the chamber, (i.e., include those going through the lower fiducial reference of chamber without interacting)

$N_o(0)$ = the number of primary particles at the upper fiducial reference such that their interaction will take place in the gate length, L_g

L_g = the gate length (i.e., the distance between the upper and lower fiducial references of the chamber)

L_c = the mean free path of the primary particles.

Hence,

$$P(0) = \frac{N_t(0)}{N_o(0)}$$

$N_t(0)$ = the total number of primary particles at the upper fiducial reference in the chamber.

Also define

N_f = the number of primary particles not interacting in the gate length (i.e., those going through the lower fiducial reference without interacting).

Assume that the number of primary particles, $dN_t(x)$, in a distance, dx, is proportional to the total number of primary particles, $N_t(x)$, and the distance, dx. The constant of proportionality will obviously turn out to be $1/L_c$, i. e., the reciprocal of the mean free path. Specifically,

$$dN_t(x) = -\frac{1}{L_c} N_t(x)\, dx \,. \qquad \text{Eq. 1}$$

Integrating Equation 1

$$N_t(x) = Ce^{-x/L_c} \qquad \text{Eq. 2}$$

where

C = constant of integration.

Substituting Equation 2 in Equation 1 and dividing by $N_o(0)$, then

$$\frac{dN_t(x)}{N_o(0)} = -\frac{1}{L_c} \frac{Ce^{-x/L_c}}{N_o(0)} \,. \qquad \text{Eq. 3}$$

The ratio in Equation 3 represents the differential probability, $dP(x)$, of observing a primary particle within the gate length, L_g. Since only that gate length is observed

$$\int_0^1 dP(x) = 1 \,.$$

Therefore,

$$\int_0^1 dP(x) = \int_0^{L_g} \frac{1}{L_c} \frac{Ce^{-x/L_c}}{N_o(0)} dx \qquad \text{Eq. 4}$$

$$= \frac{C}{N_o(0)} \left(1 - e^{-L_g/L_c} \right)$$

$$= 1 \quad .$$

The constant, C , may then be evaluated

$$C = \frac{N_o(0)}{1 - e^{-L_g/L_c}} \qquad \text{Eq. 5}$$

Substituting Equation 5 in Equation 2

$$N_t(x) = \frac{N_o(0)\, e^{-x/L_c}}{1 - e^{-L_g/L_c}} \qquad \text{Eq. 6}$$

When $x = 0$ Equation 6 becomes

$$N_t(0) = \frac{N_o(0)}{1 - e^{-L_g/L_c}} \qquad \text{Eq. 7}$$

or

$$N_t(x) = N_t(0)\, e^{-x/L_c} \qquad \text{Eq. 8}$$

Since by definition, the number of primary particles not interacting in the gate length is N_f ,

$$N_f = N_t(L_g)$$

and by substitution in Equation 6

$$N_f = \frac{N_o(0)\, e^{-L_g/L_c}}{1 - e^{-L_g/L_c}} \qquad \text{Eq. 9}$$

or

$$N_f = N_t(0)\, e^{-L_g/L_c} \quad . \qquad \text{Eq. 10}$$

Since the total number of particles is conserved

$$N_t(x) = N_o(x) + N_f \quad . \qquad \text{Eq. 11}$$

Substituting Equations 8 and 9 in Equation 11

$$N_o(x) = N_t(0)(e^{-x/L_c} - e^{-L_g/L_c}) \quad . \qquad \text{Eq. 12}$$

When $x = 0$, Equation 12 becomes

$$N_o(0) = N_t(0)\,(1 - e^{-L_g/L_c}) \quad . \qquad \text{Eq. 13}$$

Hence,

$$P(0) = \frac{N_t(0)}{N_o(0)}$$

$$= \frac{1}{1 - e^{-L_g/L_c}} \qquad \text{Eq. 14}$$

or in terms of the original definition of P (x)

$$P(x) = P(0)\, e^{-x/L_c} \qquad \text{Eq. 15}$$

which can also be seen directly from Equation 8.

In the event that the gate length is variable, Equation 14, and hence Equation 8 must be modified to account for that variation. The differential probability thus becomes

$$\left[dP(x)\right]_i = -\left[\frac{1}{L_c}\,\frac{e^{-x_i/L_c}}{1 - e^{-(L_g)_i/L_c}}\right] dx_i \qquad \text{Eq. 16}$$

For an independent number of interactions obeying the foregoing probability relation, the probability of obtaining a particular set of experimental data is proportional to the product of the differential probabilities of Equation 16.

Define the likelihood function as the expression in the bracket on the right hand side of Equation 16.

$$L = \prod_{i=1}^{N} \frac{1}{L_c} \frac{e^{-x_i/L_c}}{1 - e^{-(L_g)_i/L_c}} \qquad \text{Eq. 17}$$

The maximum likelihood procedure consists of finding the parameter, L_c, which maximizes the likelihood function, L. Because of the nature of the product, it is more convenient to maximize ln L. That is,

$$\frac{\partial \ln L}{\partial L_c} = 0 \quad . \qquad \text{Eq. 18}$$

Carrying out the differentiation one obtains

$$L_c = \frac{1}{N} \sum_{i=1}^{N} \left[x_i + \frac{(L_g)_i}{e^{(L_g)_i/L_c} - 1} \right] . \qquad \text{Eq. 19}$$

In the case of constant gate length this reduces to

$$L_c = \frac{L_g}{e^{L_g/L_c} - 1} + \frac{1}{N} \sum_{i=1}^{N} x_i \quad . \qquad \text{Eq. 20}$$

The graph for the foregoing relation is shown in Figure D on the following page.

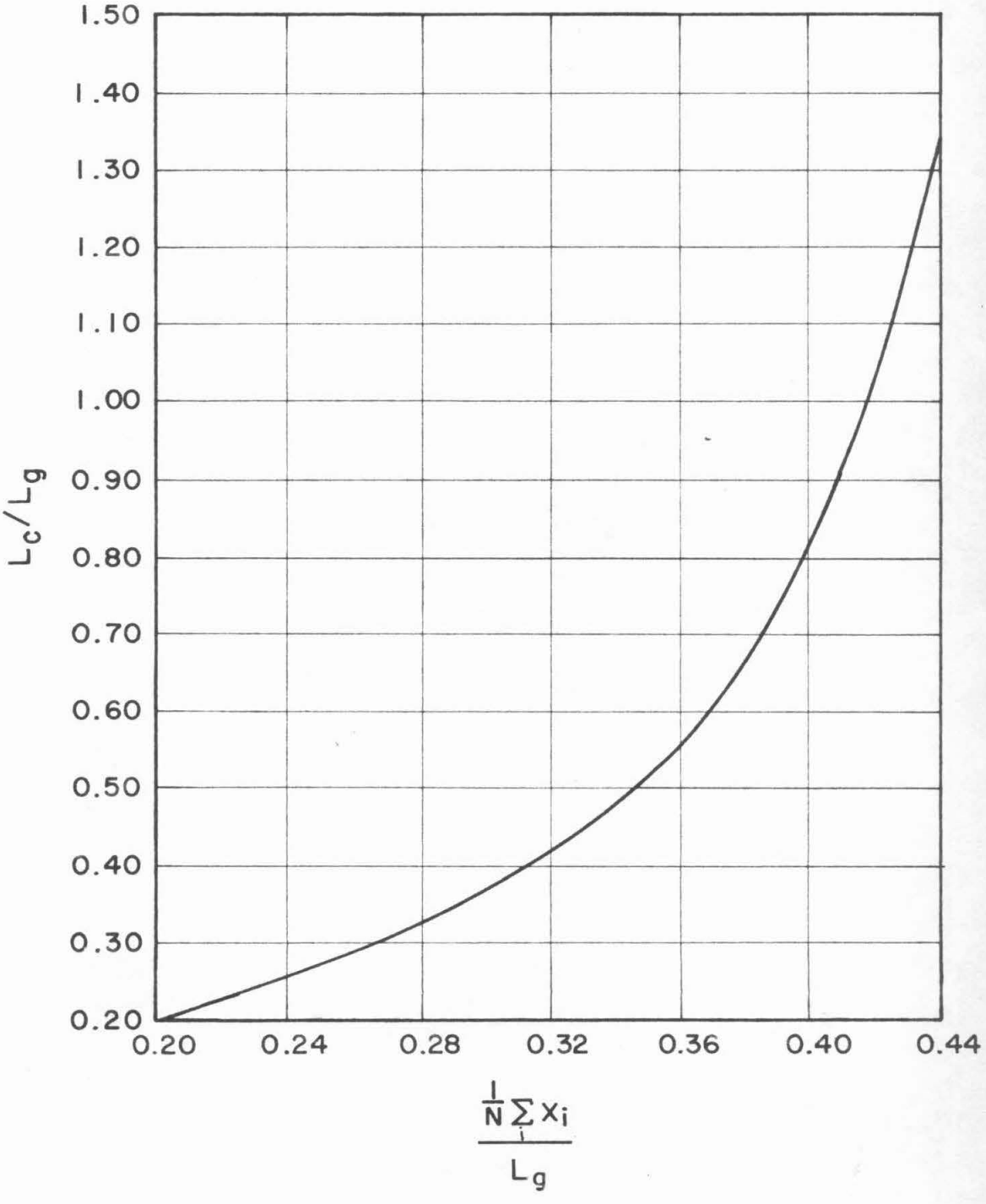

Figure D. Maximum Likelihood Graph

The standard deviation, σ , is given in terms of the second derivative of the likelihood function as follows

$$\frac{\partial^2 L}{\partial L_c^2} = - \frac{1}{\sigma^2} \quad . \qquad \text{Eq. 21}$$

Hence carrying out the differentiation one obtains

$$\sigma = L_c \left[\sum_{i=1}^{N} \left\{ 1 - \frac{(L_g)_i^2}{L_c^2} \frac{e^{(L_g)_i/L_c}}{\left(e^{(L_g)_i/L_c} - 1 \right)^2} \right\} \right]^{-1/2} . \qquad \text{Eq. 22}$$

In the case of constant gate length this reduces to

$$\sigma = L_c \left[N \left\{ 1 - \frac{L_g^2}{L_c^2} \frac{e^{L_g/L_c}}{\left(e^{L_g/L_c} - 1 \right)^2} \right\} \right]^{-1/2} . \qquad \text{Eq. 23}$$

REFERENCES

1. Wilson, C.T.R., Proc. of Roy.Soc. 85A, 285, (1911)

2. Blackett, P.M.S. and Occhialini, G.P.S., Proc. Roy.Soc. 139 A, 699, (1933)

3. Carlson, J.F. and Oppenheimer, J.R., Phys. Rev. 51, 220, (1937)

4. Bhabha, H.J. and Heitler, W., Proc. Roy. Soc. 159, 432, (1937)

5. Rossi, B. and Griesen, K., Rev. Mod. Phys. 13, 240, (1941)

6. Heitler, W., Quantum Theory of Radiation, Oxford Univ. Press (1948)

7. Landau, L. and Rumer, G., Proc. Roy. Soc. 166, 213, (1938)

8. Rossi, B., High Energy Particles, Prentice-Hall Inc., (1952)

9. Janossy, L., Cosmic Rays, Oxford Univ. Press, (1950)

10. Heisenberg, W., Zeit. Phys. 126, 569, (1949)

11. Lewis, H.W., Oppenheimer, J.R. and Wouthuysen, S.A., Phys. Rev. 73, 127, (1948)

12. Fermi, E., Phys. Rev. 81, 683, (1951)

13. Fermi, E., Progr. Theor. Phys. 5, 570, (1950)

14. Belenkii, S.Z. and Landau, L., Nuovo Cim. 1, 3, 15, (1956)

15. Hazen, W.E., Heineman, R.E. and Lennox, E.S., Phys. Rev. 86, 198, (1952)

16. Castagnoli, C., Cortini, G., Franzinetti, C., Manfredini, A. and Moreno, D., Nuovo Cim. 10, 9, 1539, (1953)

17. Kaneko, S., Kusumoto, O., Matsumoto, S. and Takahata, M., Proc. of Moscow Cosmic Ray Conf. 1, 107, (1960)

18. Teucher, M.W., Lohrmann, E., Haskin, D.M. and Schein, M., Proc. of Moscow Cosmic Ray Conf. 1, 26, (1960)

19. Udgaonkar, M. and Gell-Mann, M., "High Energy Nuclear Scattering and Regge Poles," To be published

20. Brenner, A.E. and Williams, R.W., Phy. Rev. 106, 1020, (1957)

21. Fisher, R.A., Trans. Roy. Soc. 222, 309, (1922)

22. Peirls, R., Proc. Roy. Soc. 149, 467, (1935)

23. Bartlett, M.S., Proc. Roy. Soc. 154, 124, (1936)

24. Alford, W.L., Ph.D. Thesis, "The Mean Lifetime of V-Particles," Cal. Tech. (1953)

25. Strassenburg, A.A., Ph.D. Thesis, "The Lifetime of the Λ^o and θ^o Particles," Cal. Tech. (1955)